

Characterisation and optimisation of superconducting microwave resonators

THIJS BOEHME

Erasmus Mundus Master of Science in Nanoscience and Nanotechnology

Promoter: Prof. Jonas Bylander

Co-promoter: Prof. Margriet Van Bael



MASTER'S THESIS IN ERASMUS MUNDUS MASTER OF SCIENCE IN NANOSCIENCE AND
NANOTECHNOLOGY

Characterisation and optimisation of superconducting microwave
resonators

THIJS BOEHME

Department of Microtechnology and Nanoscience
Quantum Device Physics
CHALMERS UNIVERSITY OF TECHNOLOGY
Gothenburg, Sweden 2016

Characterisation and optimisation of superconducting microwave resonators
THIJS BOEHME

© THIJS BOEHME, 2016

ISSN 1652-8557
Department of Microtechnology and Nanoscience
Quantum Device Physics
Chalmers University of Technology
SE-412 96 Gothenburg
Sweden
Telephone: +46 (0)31-772 1000

Cover:

Micrograph of a sample with four resonators, with two sets of widths and a meandered and not meandered version for each set.

Chalmers Reproservice
Gothenburg, Sweden 2016

Characterisation and optimisation of superconducting microwave resonators
Master's thesis in Erasmus Mundus Master of Science in Nanoscience and Nanotechnology
THIJS BOEHME
Department of Microtechnology and Nanoscience
Quantum Device Physics
Chalmers University of Technology

ABSTRACT

In this master's thesis, I present the design, fabrication, and characterisation of superconducting microwave resonators. These resonators are quarter-wavelength coplanar waveguide resonators, operating at resonance frequencies between 4 GHz and 8 GHz. This kind of resonator is a key component in several applications, ranging from quantum computation devices to parametric amplifiers. Minimising the losses (achieving high internal quality factors) in these resonators is important to maximise performance of the applications they are used for. During the thesis work, we have studied several possible changes to improve the resonator quality.

Fabrication of the resonators was done in the Nanofabrication Laboratory at Chalmers University of Technology, and consist of the following steps: cleaning a sapphire or silicon wafer, depositing a layer of superconducting niobium, photolithography, and etching the waveguide. We then measured the resonators in a cryogen-free dilution refrigerator, at a temperature of 10 mK. The measurements consisted of a power sweep, in order to quantify the quality factor at high and low excitation powers. As an example, the first resonator we fabricated had a quality factor of 4.3×10^4 at high power (about 10^5 photons in the resonator), and quality factor of 3.7×10^4 at the single-photon level.

We then investigated different loss mechanisms that we expect to negatively affect the quality factor, and how to reduce this loss. Firstly, to reduce radiation losses and magnetic vortex losses, we reduced the lateral dimensions of the resonator. Secondly, as two-level system (TLS) losses are believed to mainly reside at the surfaces of the materials and interfaces between them, we etched into the substrate to effectively move a part of the TLS away from the resonator. We also studied the effect of the meandering of the resonator on the quality factor, as well as using two different etching gasses.

By gathering all this data, we were then able to compare the different combinations to see the effect of the changing parameters. In conclusion, the reduced lateral dimensions and the removal of part of the substrate indeed reduce the losses, as expected from the theory. We also found interesting behaviour with regards to the meandering, namely that having a meandered structure negatively affects the quality factor.

Combining all results, we can give a guideline for the fabrication of resonators in the future, which gave us a quality factor up to 4.9×10^5 at high excitation power, and 3.0×10^5 at the single photon level.

Keywords: Superconducting resonators

ACKNOWLEDGEMENTS

First and foremost, I wish to thank my promoter, Prof. Jonas Bylander, for having me do this thesis with him. His knowledge, patience and guidance have helped me during the research and the writing of this thesis.

Secondly, I want to express my gratitude towards my daily supervisor, Andreas Bengtsson, for spending a lot of time designing, fabricating, measuring and discussing resonators with me.

Next, I would like to thank Prof. Margriet Van Bael for agreeing to be my co-promoter.

Many thanks to all the members of the Experimental Mesoscopic Physics Group for welcoming me in their midst, creating a very good work environment and having discussions on various topics, and to the cleanroom staff for training me on several tools.

I would also like to thank the board of the Erasmus Mundus Master of Science in Nanoscience and Nanotechnology, for granting me this opportunity to study abroad, and Erasmus+ for my scholarship.

I would like to thank friends and family for their support, and in particular my parents. They made it possible to take this opportunity and encouraged me from start to finish.

Last but certainly not least, my amazing girlfriend Liessa. Regardless of the distance between us, she was always there for me, and without her support and love this wouldn't have been possible.

Thijs Boehme
Gothenburg, June 2016

Contents

Abstract	i
Acknowledgements	iii
1 Introduction	1
1.1 Motivation	1
1.2 Structure of the thesis	1
2 Theory	3
2.1 Resonators and transmission line theory	3
2.1.1 Resonators	3
2.1.2 Transmission line theory and fitting functions	3
2.1.3 Additional fit parameters	5
2.1.3.1 Impedance Mismatching	7
2.1.3.2 Amplitude background	7
2.1.3.3 Electrical length	7
2.2 Loss Mechanisms	7
2.2.1 Two-level systems	7
2.2.2 Radiation	9
2.2.3 Vortex pinning	9
2.2.4 Other losses	10
2.2.5 General loss equation	10
3 Experiments	11
3.1 Design	11
3.1.1 Structure	11
3.1.2 Centre line and gap width	12
3.1.3 Meandering	12
3.2 Materials	13
3.3 Fabrication	13

3.3.1	Deposition of superconductor	14
3.3.2	Deposition of contacts	14
3.3.3	Etching of the waveguide	15
3.4	Cryogenic measurements	19
3.4.1	Cryostat	19
3.4.2	Setup	19
4	Results	21
4.1	Measurement and fitting flow	21
4.1.1	Measurements	21
4.1.2	Fitting	22
4.2	Results and discussion	27
4.2.1	Sample overview	27
4.2.2	Centre conductor and gap width	27
4.2.3	Meandering	27
4.2.4	Etching	27
5	Conclusion	33
	Appendices	35
A	Recipes	35
A.1	Wafer cleaning	35
A.1.1	Sapphire wafer	35
A.1.2	Silicon wafer	35
A.2	Lift-off	35
A.3	Etching	36
A.4	Dicing	37
B	Transmission Fitting Function	38
B.1	Analogous to the reflection fitting function	38
B.2	Alternative derivation	39
B.3	Alternative form	40
	References	40

Part 1

Introduction

1.1 Motivation

Superconducting coplanar waveguide (SCPW) resonators are a key component in several applications, ranging from superconducting qubits, quantum memories and quantum computer architectures in general, to narrow bandwidth microwave filters, electromagnetic radiation detectors, single-photon detectors and generators, and quantum limited parametric amplifiers [1, 2].

Achieving a high quality factor (Q -factor) is important to maximise photon lifetimes in these resonators. Q -factors up to several million at high excitation power and a million at single-photon excitation power have been achieved [3].

The goal with this thesis work is to combine several improvements presented in the literature and implement them for the resonators fabricated in the quantum device physics (QDP) research group at Chalmers University of Technology. While not all possible improvements were tested during this work, I achieved an improvement up to one order of magnitude at high power, and other improvements are proposed for future work.

1.2 Structure of the thesis

In Part 2, we will look at the necessary theory. This includes the derivation of fitting functions to extract quality factors from the data, as well as an overview of the loss mechanism we expect in these devices.

Part 3 is the main matter of the thesis, in which we will look at the design of the resonators used for the measurements, the fabrication of the devices, and the setup of the measurements. Here we will also discuss the parameters we chose to change and what effect we expect these changes to have.

In Part 4 we will look at the workflow we maintained during this work, and at the results we achieved. We will then compare the results to our expectations, and discuss the results in general.

We then end the thesis with a conclusion and an outlook on further research.

Part 2

Theory

In this part, we will look at the necessary theory.

In Sec. 2.1 we derive functions that we will use in Part 4 to fit the data and extract quality factors. This requires us to look at transmission line theory and apply it to the setup we use, as well as add specific fitting parameters to account for parasitic effects that will occur in real life experiments.

In Sec. 2.2 we list the most important loss mechanisms that will be present in our devices. We will look at how to distinguish between the different losses, and their respective dependencies on physical quantities.

2.1 Resonators and transmission line theory

2.1.1 Resonators

The device that we measured during the thesis is a quarter-wavelength superconducting resonator. The resonator itself is a coplanar waveguide resonator, having a centre conductor separated from a ground plane on top of a dielectric substrate (Fig. 2.1). This structure is similar to a cut-out or flattening of a coaxial cable. The resonators are quarter-wavelength resonators, i.e. shorted to the ground plane at one end and with the other end open.

The resonator will be used as either a series or parallel element with a transmission line, and will then exhibit some change in transmission or reflection behaviour at its resonance frequency. From the resonance behaviour, the quality factor Q and losses $\delta = 1/Q$ can be determined by fitting a theoretical model to the measurement data.

2.1.2 Transmission line theory and fitting functions

To derive fitting functions one needs to start with an equivalent electrical diagram. First, let's consider the reflection of a one-port sample (Fig. 2.2a). By modelling the coplanar waveguide with an equivalent circuit (Fig. 2.2b), where the resistance R_R represents the losses in the resonator, one can derive the



Figure 2.1: *Cross-section (left) and top view (right) of a quarter wavelength coplanar waveguide with the centre conductor and ground plane (yellow) on top of a substrate (hashed). The centre conductor of width W is separated from the ground plane by gaps of width S . The resonator is terminated by an open end on one side and a shorted end on the other.*

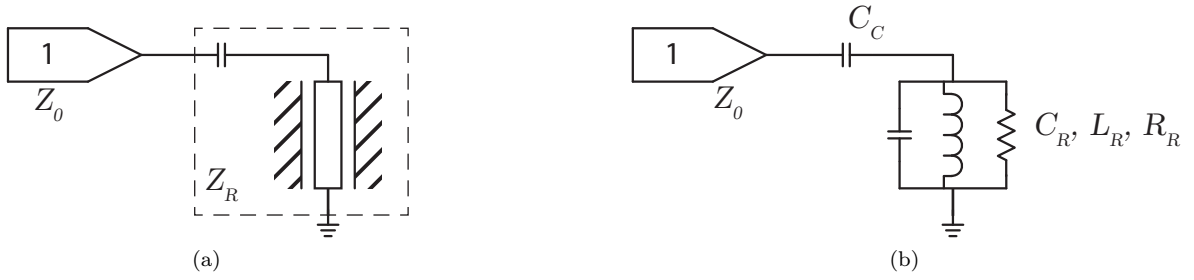


Figure 2.2: Schematic representation of a reflection setup, with the resonator consisting of the coplanar waveguide and coupling capacitor indicated with a dashed box (left), and with the equivalent circuit for the coplanar waveguide (right).

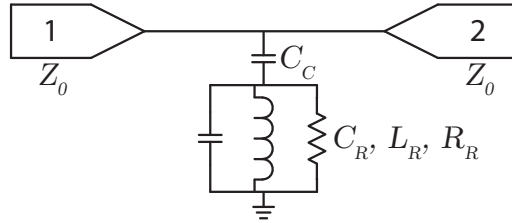


Figure 2.3: Schematic representation of a two-port sample, also known as a hanging resonator, with equivalent circuit of the coplanar waveguide.

equation for the reflection coefficient S_{11} :

$$S_{11} = \frac{Z_R - Z_0}{Z_R + Z_0},$$

and by filling in all elements we get [4]:

$$S_{11} = \frac{\delta f^2 + \frac{1}{4}f_0^2 \left(\left(\frac{1}{Q_i} \right)^2 - \left(\frac{1}{Q_e} \right)^2 \right) + if_0\delta f \frac{1}{Q_e}}{\delta f^2 + \frac{1}{4}f_0^2 \left(\frac{1}{Q_i} + \frac{1}{Q_e} \right)^2}, \quad (2.1)$$

where $\delta f = f_0 - f$ is the detuning from the resonance frequency with the resonance angular frequency $\omega_0 = 2\pi f_0 = 1/\sqrt{L_R(C_R + C_C)}$, internal quality factor $Q_i = \omega_0 R_R (C_R + C_C)$, and external quality factor $Q_e = (C_R + C_C) / (Z_0 C_C^2 \omega_0)$. The internal quality factor Q_i is related to losses inside the resonator, while the external quality factor Q_e is related to photons leaving the resonator through the coupling capacitor.

With a two-port device, both reflection and transmission can be measured. Only transmission will be investigated, as this behaves more similarly to the one-port reflection. Thus for the rest of the thesis, whenever there is mention of reflection and transmission, reflection will be that of a single-port device, while transmission (by definition) refers to a two-port device.

A derivation for the transmission coefficient S_{21} analogous to that of the reflection coefficient (Fig. 2.3) is done in Appendix B, beginning from

$$S_{21} = \frac{2Z_R}{2Z_R + Z_0}$$

to obtain

$$S_{21} = \frac{\delta f^2 + f_0^2 \frac{1}{4Q_i} \left(\frac{1}{Q_i} + \frac{1}{Q_e} \right) + i f_0 \delta f \frac{1}{2Q_e}}{\delta f^2 + \frac{1}{4} f_0^2 \left(\frac{1}{Q_i} + \frac{1}{Q_e} \right)^2}. \quad (2.2)$$

One could also start from the fact that $S_{21} - S_{11} = 1$, with

$$S_{11} = \frac{-Z_0}{2Z_R + Z_0},$$

to derive an equivalent formula

$$S_{21} = 1 - \frac{Q_l/Q_e}{1 + i2Q_l(\omega - \omega_0)/\omega_0},$$

where the loaded quality factor $Q_l = (1/Q_i + 1/Q_e)^{-1}$, or even

$$S_{21}^{-1} = 1 + \frac{Q_i/Q_e}{1 + i2Q_i(\omega - \omega_0)/\omega_0},$$

which both are used in the literature [2, 3, 5–8].

Depending on the ratio of the internal and external quality factors, three distinct regimes can be identified. Firstly, when $Q_i < Q_e$ the resonator is undercoupled, which means that the losses in the resonator are large and photons dissipate faster in the resonator than they are entering and leaving through the coupling capacitor, which is indicated with the external quality factor. Secondly, when $Q_i = Q_e$ the resonator is critically coupled. Lastly, when $Q_i > Q_e$ the resonator is overcoupled, meaning that the loss in the resonator is small enough that photons can easily enter and leave the system before they are dissipated. The critically coupled and overcoupled regime are thus the two preferred regimes to work in.

The magnitude and phase response of both reflection [Eq. (2.1)] and transmission [Eq. (2.2)] are shown in Fig. 2.4. In the case of reflection at critical coupling, the magnitude response will drop to zero at the resonance frequency and the phase will see a 180° phase shift. When overcoupled, the magnitude response will not be zero at the resonance frequency, but a full 360° phase shift will be observed.

In the case of transmission, the magnitude response will only drop to 0.5 (or –6 dB) at critical coupling. In the theoretical case of infinite Q_i , the transmission response would look similar to the critically coupled reflection response.

Since the transmission goes to unity for frequencies away from the resonance frequency, multiple resonators can be frequency multiplexed on a single device by designing the resonance frequency of every resonator to be different from the others. The total transmission function would then be a product of the individual transmission functions, but by only looking at a small window around the resonance frequency of a particular resonator, the other resonators can be ignored and Eq. (2.2) can still be used as the fitting function.

2.1.3 Additional fit parameters

The theoretical model is very nice, but the fitting functions introduced in the previous section often do not fit actual data very nicely for several reasons. Those theory-experiment discrepancies are explored in this section and adaptations to the fitting functions to account for these discrepancies are proposed. In Fig. 2.5, a visual comparison is given how these additional fitting parameters change the complex response of a reflection measurement.

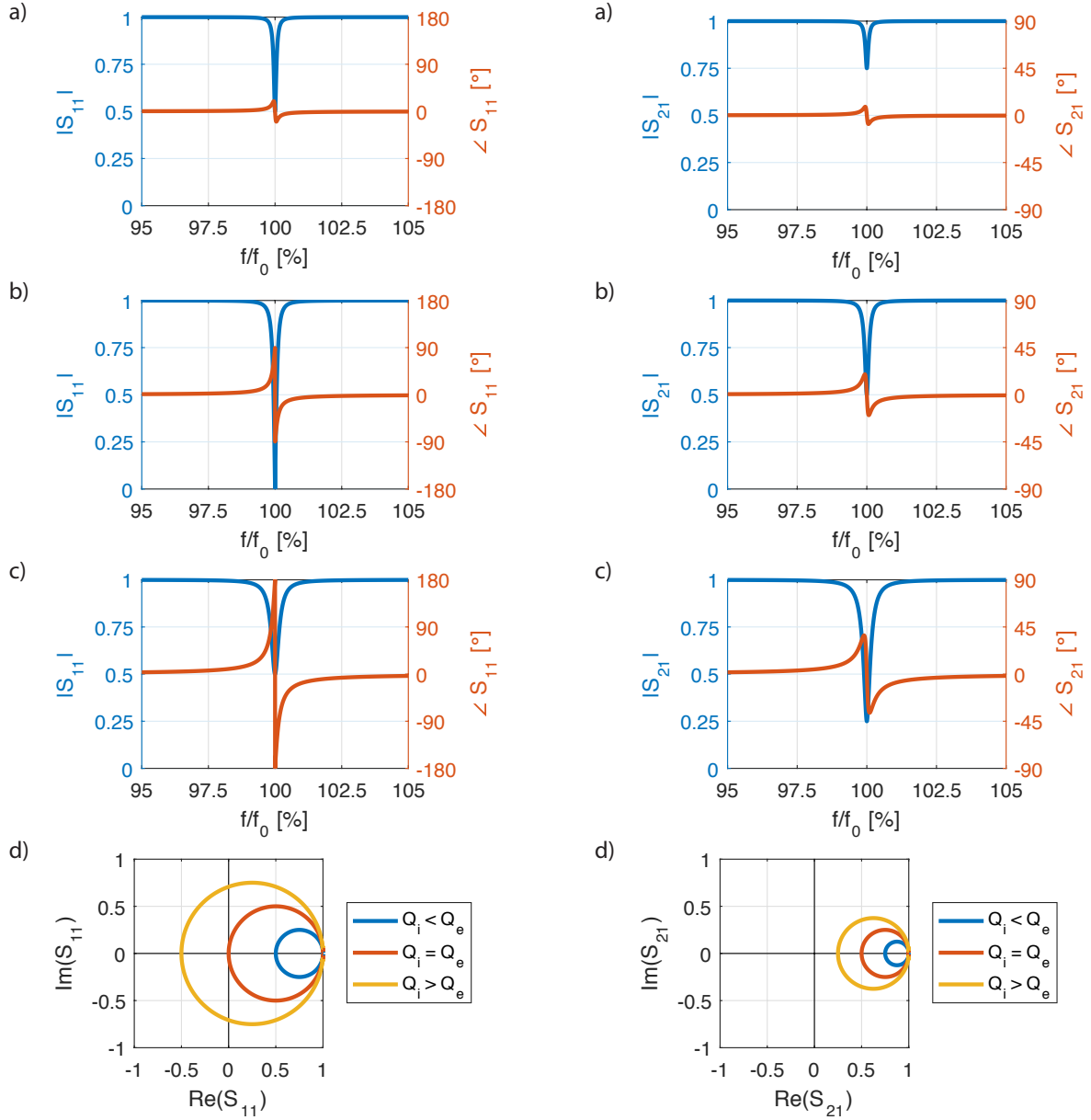


Figure 2.4: Reflection (left) and transmission (right) response for the different coupling regimes. a) Undercoupled b) Critically coupled c) Overcoupled d) The response in the complex plane. $Q_i = 1 \times 10^3$ and $Q_e/Q_i = 3, 1, 1/3$ for the three respective regimes.

2.1.3.1 Impedance Mismatching

Exact impedance matching of the in- and output-port have proven to be difficult to achieve in actual physical devices. On top of that, inductive effects in the feedline have been assumed very small ($\ll C_C Z_0$) but do influence the reflection or transmission response of the devices. Mismatching results in asymmetry of the response. This mismatching can be accounted for in three different, equivalent ways [7]. We chose to model the mismatching as a complex loading of the resonator, quantified by adding an imaginary part to the external quality factor Q_e . This translates into a scaling and an asymmetry of the magnitude and phase response, or a scaling and a rotation around the resonance point in the complex plane (Fig. 2.5b).

We can then define the coupling quality factor Q_c as [3]:

$$Q_c^{-1} = \text{Re} \left(\frac{1}{Q_e} \right). \quad (2.3)$$

2.1.3.2 Amplitude background

Any attenuation that is not accounted for will lead to an offset in the amplitude response of the signal. There may also be some frequency dependent attenuation in the components of the setup, leading to a non-constant background signal.

Ideally, one would measure the background and subtract that signal from the response of the device. However, in the setup used here this is not possible. One would need to be able to turn off the resonator, or be able to change the resonance frequency temporarily, which is not something that is possible in these simple devices. To compensate for this, a first order approximation of the background is done by adding an overall amplitude factor A and a linear variation α [3]:

$$S'_{21} = A \left(1 + \alpha \frac{f - f_0}{f_0} \right) S_{21}. \quad (2.4)$$

In the complex plane, this translates into a scaling with reference to the origin, and a splitting at the resonance frequency as the response goes to $\pm\infty$, asymptotic to the x-axis (Fig. 2.5c).

2.1.3.3 Electrical length

There usually is some phase propagation delay to and from the sample, also known as the electrical length. This is accounted for by adding frequency-independent and -dependent phase factors ϕ_0 and ϕ_f , respectively, to the response [3]:

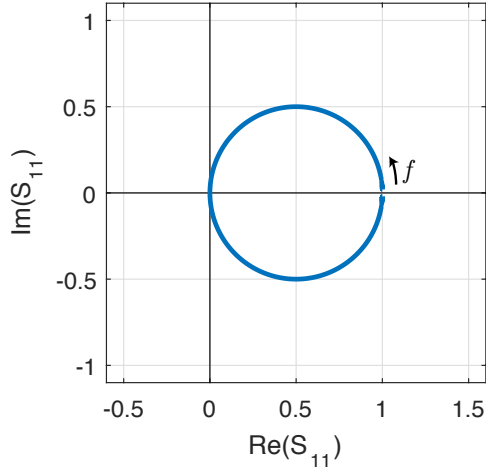
$$S'_{21} = S_{21} e^{i(\phi_0 + \phi_f f)}. \quad (2.5)$$

In the complex plane, the frequency-independent angle will simply rotate the response around the origin, while the frequency-dependent angle will effectively ‘stretch’ the response in both directions around the origin (Fig. 2.5d).

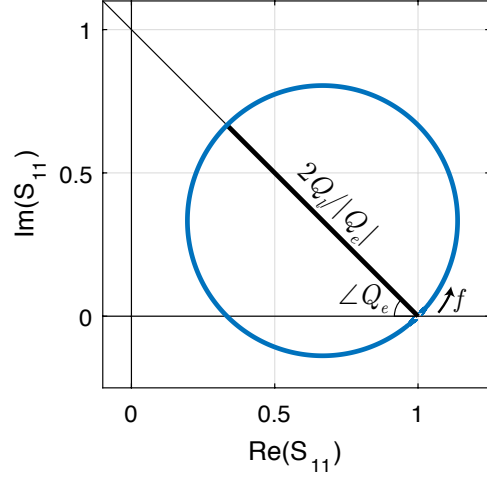
2.2 Loss Mechanisms

2.2.1 Two-level systems

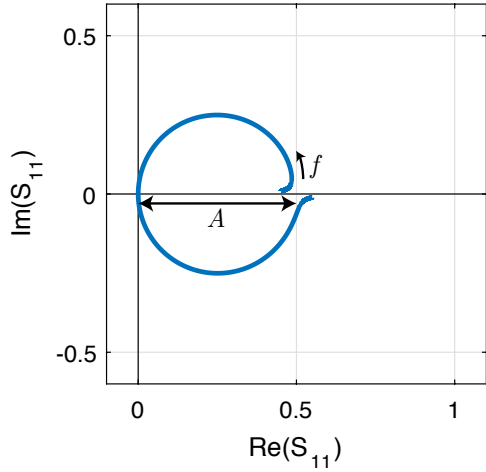
Two-level systems (TLS) are systems present mainly at the interfaces between metal and vacuum, metal and substrate, and substrate and vacuum. They consist of two states, a ground and excited state, which can couple to the electric field in the resonator. The system can then be excited, and therefore dissipate some energy and contribute to the losses. At high temperatures and powers these TLS are saturated



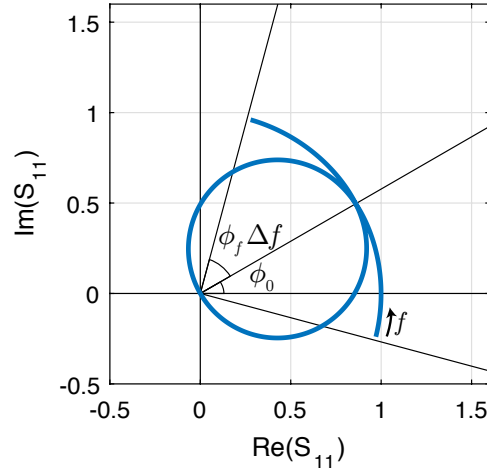
(a) The response in the complex plane without any additional fitting parameters, for visual comparison. $Q_i = Q_e = 1 \times 10^3$.



(b) The response in the complex plane with impedance mismatching, quantised by a complex external quality factor $Q_e = 10^3 + 10^3i$, resulting in a scaling of the response due to the change in loaded quality factor Q_l and external quality factor Q_e , and a rotation along the resonance point with an angle $\angle Q_e$.



(c) The response in the complex plane with amplitude background parameters $A = 0.5$ and $\alpha = 10$, resulting in a scaling with respect to the origin with factor A , and a splitting at the resonance frequency point bending the curve towards the x -axis.



(d) The response in the complex plane with electrical length parameters $\phi_0 = \pi/6$ and $\phi_f \Delta f = \pi/4$, where $\Delta f = 5\% f_0$ is half of the frequency range over which the response is plotted.

Figure 2.5: The reflection response in the complex plane without and with the different additional fitting parameters.

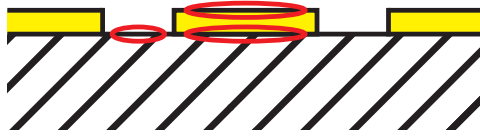


Figure 2.6: Schematic drawing of the location where TLS are mainly present. Indicated are the three different interfaces: metal-vacuum, metal-substrate, and substrate-vacuum.

either by thermal or signal population, whereas in the low-power regime (single photon) and at low temperatures they are not, resulting in a larger loss.

TLS losses are thus power dependent through the equation

$$\delta_{\text{TLS}}(P_r, T) = \delta_{0,\text{TLS}} \frac{\tanh(\hbar\omega_r/2k_B T)}{\sqrt{1 + (P_r/P_c)^{\beta/2}}}, \quad (2.6)$$

where $\delta_{0,\text{TLS}}$ is the low power and low temperature limit due to unsaturated TLS, \hbar is the reduced Planck constant, ω_r is the resonance angular frequency, k_B is the Boltzmann constant, T is the temperature, P_r is the power circulating inside the resonator, P_c a characteristic power depending on the TLS properties and geometry of the resonator above which the TLS start to saturate, and β a fitting parameter accounting for the fact that the power inside the resonator is not uniform along and orthogonal to the resonator trace, and thus not simply equal to P_r [1, 5, 9].

Because TLS losses are the only power dependent type of loss and the dominant loss mechanism at the single-photon regime, reducing these has the priority in improving the Q -value.

2.2.2 Radiation

Radiation losses analytically scale by

$$\delta_{\text{rad}} \propto \left(\frac{W + S}{L} \right)^2, \quad (2.7)$$

where L is the length of the resonator, W is the centre line width, and S is the gap width between centre conductor and ground plane [10]. This relation tells us that the radiation losses increase with the widths of both the centre conductor and the gap, and with the resonance frequency. So in order to reduce radiation losses, we should try to keep the resonance frequency low, as well as reducing the line and gap widths.

2.2.3 Vortex pinning

While the Meissner effect of complete expulsion of an external magnetic field is a well-known characteristic of superconductors, magnetic flux can still be trapped at grain boundaries or other defects, especially for a type-II superconductor like niobium. Trapped vortices of quantised magnetic flux in the superconducting trace can result in a reduction of the Q -value [11], especially when they reside in the centre conductor and create small current loops. Additionally, the movement of magnetic vortices will also dissipate some of the energy.

This movement of magnetic vortices can be prohibited by creating small holes in the superconductor, which will trap the vortices. Moreover, the creation of vortices themselves can be avoided. While cooling down through the critical temperature of the superconductor T_c , vortices will nucleate when

the temperature nears T_c , seek out the configuration that lowers the free energy of the system, and will freeze out at a temperature very close to T_c and remain pinned throughout the cool-down. However, for vortices to nucleate during the cool-down, the magnetic field needs to be above a certain threshold B_{th} . In the resonator, this threshold field has been theoretically and experimentally shown to follow

$$B_{th} \propto \frac{1}{W^2} \ln W,$$

where W is the width of the centre line conductor [12]. So, by reducing the width W , this threshold field can be high enough to avoid nucleation of vortices.

2.2.4 Other losses

Many other losses may be present, but are negligible in comparison to the losses discussed up to this point. One of these losses is the resistive, or ohmic, loss which is easily understood to be negligible due to the properties of superconductors.

2.2.5 General loss equation

Unfortunately, performing temperature sweeps as well as magnetic flux sweeps was not in the scope of this project. As a result, distinguishing between power-independent losses is not possible and we will only be able to fit our data to

$$\delta_i = \delta_{TLS} + \delta_c, \tag{2.8}$$

where δ_{TLS} is given by equation (2.6), and $\delta_c = \delta_{rad} + \delta_{vortex} + \dots$ is the term combining all power-independent losses like radiation and vortex pinning losses.

Part 3

Experiments

In this part of the thesis, we will go through some aspects of the experimental side of the research.

Beginning in Sec. 3.1, we go through some of the design elements of the devices that need to be considered and look at the design parameters that were varied between different implementations of the devices.

In Sec. 3.2, we take a quick look at the different materials that were used in this project.

Next, in Sec. 3.3, some key fabrication processes are listed, as well as some fabrication parameters that were varied.

In Sec. 3.4, we look at the measurement setup that was used to obtain the results of the next part.

3.1 Design

3.1.1 Structure

Using the quarter-wavelength transmission structure is beneficial for one important reason. Away from resonance, the transmission response is practically unity, allowing for multiple resonators to be measured with a single feed line, using frequency domain multiplexing. Having multiple resonators per chip then not only reduces material and processing cost per resonator, it also allows testing several design variations on one chip, and thus in one cool-down, reducing the number of measurement lines in the cryostat or the amount of times the cryostat needs to be cooled down, again reducing cost in terms of cooling power, and reducing the overall time to measure multiple resonators.

The multiplexing is limited by some factors:

- The resonance frequencies need to be separated enough to not interfere with each other, which is also called frequency crowding. From the definition of the quality factor Q_l , the full width at half maximum (FWHM) is given by [10]:

$$\Delta\omega = \omega_0/Q_l,$$

which, for a resonator at 6 GHz with a Q_l of 1×10^5 , results in a FWHM of 60 kHz. The frequency separation needs to be several times this value.

- The coupling Q_c induces a frequency shift of the resonance frequency. Theoretically, this shift follows [10]:

$$\Delta\omega_0(\%) = -\sqrt{\frac{2}{\pi Q_c}},$$

which, for a resonator with a Q_c of 1×10^5 , results in a shift of -0.25% , which, for a resonance frequency of 6 GHz, is equal to a shift of -15 MHz. Unfortunately, small variations in the fabrication of the coupling have a large effect on this shift, which is hard to quantify in the overall scheme.

- The precision of the fabrication of the resonator determines how precise the resonance frequency is set. For the tool used in this thesis the resolution is 700 nm. The length needed for a wanted resonance frequency (disregarding kinetic inductance effects) is given by [10]:

$$l = \frac{c}{4f_0} \sqrt{\frac{2}{1 + \epsilon}},$$

Table 3.1: Used values for the centre line and gap widths and the simulated impedance at the resonance frequency for these values for niobium on sapphire and silicon. A blank entry ('-') indicates a width pair that is not used for that particular substrate.

Centre line width [μm]	Gap width [μm]	Simulated impedance at resonance frequency [Ω]	
		Sapphire	Silicon
3	2	57.58	51.39
10	5	50.62	45.55
15	7	48.96	-
25	12	49.98	-

giving a length of 5 mm for a resonance frequency of 6 GHz when using a sapphire substrate. The precision due to the lithography is then $f_0\delta L/L = 750$ kHz.

- The available frequencies is limited by the bandwidth of the attenuators and amplifiers used in the setup, which here is 4 GHz to 8 GHz. This translates into lengths of quarter wavelength resonators ranging from 3.75 mm to 7.5 mm.
- Finally, and the most constricting factor in this case, is the available space on the chip. The size of the chips used in this thesis is 5×7 mm². Typically, up to four resonators can easily be fit on these chips.

3.1.2 Centre line and gap width

As discussed in Sec. 2.2, reducing the centre line and gap width should reduce both magnetic vortex losses and radiation losses.

While technically not necessary, we kept a 50Ω impedance for the resonator at the resonance frequency. Simulations using MICROWAVE OFFICE show that this translates closely to a 2:1 ratio of centre line versus gap width for sapphire, and to a 5:3 ratio for silicon. While the fabrication resolution is $0.7 \mu\text{m}$, I was recommended to round dimensions to a resolution of $1 \mu\text{m}$. Consequently, due to this rounding and the ratios for the different substrates not differing much, the same dimensions for the resonators were used on both substrates. The used values for the centre line and gap widths are listed in Table 3.1, together with the simulated impedance of the resonator for a sapphire substrate. As can be seen in the table, the fact that the same dimensions were used should not pose a big issue as the impedance in all cases is fairly close to 50Ω .

3.1.3 Meandering

Meandering of the resonators is often necessary to fit devices on a single chip. As the devices are very simple in this thesis, sometimes including only a single resonator on a chip, meandering could be avoided, as the chip size is fixed to fit in the measurement boxes.

In a series of samples, we looked at the effect of meandering on the quality by having pairs of resonators on a chip, only differing in resonance frequency and the structure (meandered or not, Fig. 3.1).

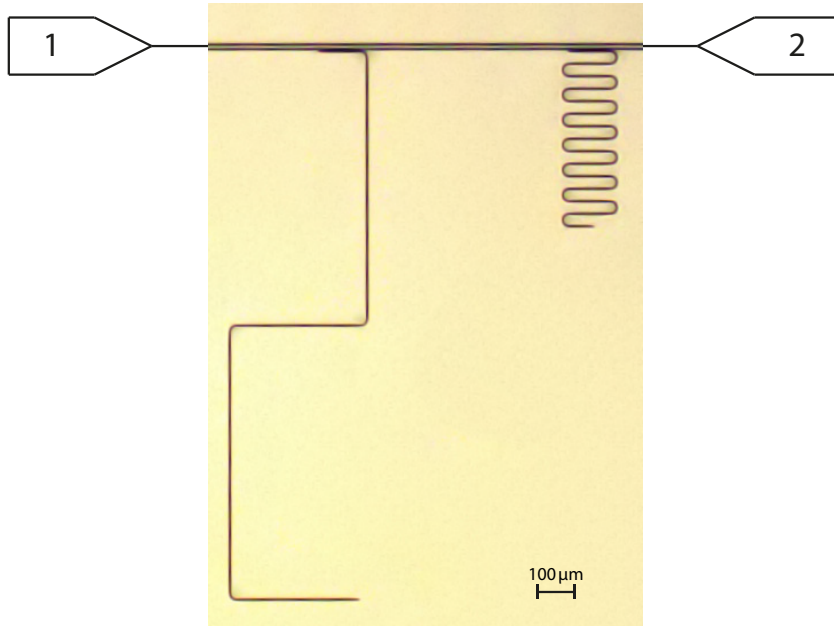


Figure 3.1: Micrograph of two resonators, with the left one not meandered and the right one meandered. Schematic ports are added to resemble the setup presented in Fig. 2.3.

3.2 Materials

While several superconducting materials and their effect on the quality have been studied [1, 13–15], the material used throughout the thesis was niobium (Nb). Nb is preferred in the QDP research group for its good superconducting properties, like the (relatively) high critical temperature $T_c = 9.25$ K and large superconducting band gap $\Delta = 1.4$ meV (equivalent temperature of 16 K) [10].

For the substrate, two materials have been used, being sapphire (Al_2O_3) and silicon (Si). The dielectric constant does not differ much between the two different substrate materials, being $\epsilon_r = 10.4$ for sapphire, and $\epsilon_r = 11.68$ for Si. Sapphire substrates are preferred over Si ones for the lower loss tangent. Sapphire also has a much higher hardness than Si, making it harder to dice cleanly (even when dicing slowly, the edges are often jagged), and harder to etch the substrate (which can be advantageous or not). Sapphire also provides better detection when etching away the superconducting layer on top.

As a result, sapphire was used for the first two samples. For the remaining samples, Si was used because of the possibility to etch into the substrate.

3.3 Fabrication

All fabrication of the devices was done in the Nanofabrication Laboratory at MC2, Chalmers. For detailed recipes, please see Appendix A.

As the devices are fairly simple, not much fabrication steps are necessary. The basic steps that were performed were

1. cleaning the wafer
2. depositing the superconducting metal

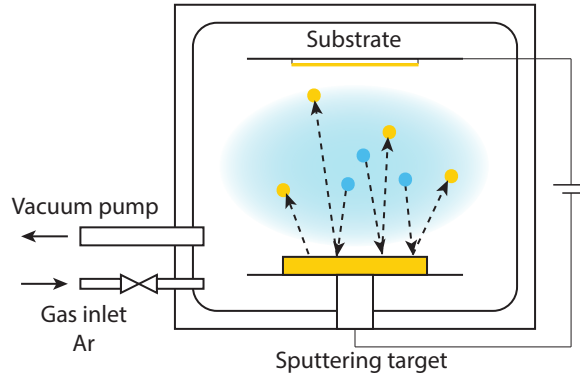


Figure 3.2: Schematic diagram of a typical DC sputtering system. The blue dots represent the Ar ions, the yellow dots and rectangles the material ejected from the sputtering target. Reprinted and modified with permission from [16].

3. depositing contacts through lithography and a lift-off process (optional)
4. lithography and etching of the waveguide structure into the superconducting metal layer
5. dicing the wafer into individual samples.

In the following sections, I will go in a bit more detail about three of the main processes: deposition of the superconductor, deposition of the contacts, and the etching of the waveguide. The superconductor and contacts are deposited with different techniques, being sputtering and evaporation, respectively.

3.3.1 Deposition of superconductor

Nb is deposited on a clean wafer using a sputter tool. A schematic of this tool is given in Fig. 3.2. Sputtering is a type of physical vapour deposition (PVD), in which particles are ejected from a target material onto the substrate by eroding the target with an argon (Ar) plasma, created by a high alternating field. The target particles will then coat the entire inside of the chamber, including the substrate that is placed there. In this work, an Nb target is used. The deposition rate is well defined. An Nb film of 90 nm was formed on the substrate.

3.3.2 Deposition of contacts

Once the Nb is sputtered onto the wafer, contacts and alignment marks can be added to the wafer. This is optional, and should theoretically not influence the Q -factor. However, more processing steps tend to degrade the Q -factor. The use of contacts can be required if one is limited in the wire bonding material. For instance, gold (Au) bonds do not adhere well to Nb, and thus require contacts, while aluminium (Al) bonds do adhere well and contacts can be omitted.

Contact pads are deposited with a lift-off process (Fig. 3.3, left). A lithography step is done first. A double layer of positive resist is spun on the wafer: a layer of lift-off resist and a layer of imaging resist, with a baking step after each layer to evaporate the solvent of the resist and harden the resist. After coating the resist on the wafer, the resist is exposed with a laser writer. Laser lithography is used to write patterns on the photoresist without the need of prefabricated masks. In this kind of maskless lithography, the ultraviolet radiation is focused as a narrow beam and directly writes the pattern, one

pixel at a time. The UV light changes the chemical structure of the resist, which makes it soluble to certain developing chemicals. Once exposed, the wafer is developed. The development will first remove the exposed parts of the imaging resist, after which it will remove the same parts of the lift-off resist, as well as creating an undercut in the layer.

The lithography step is followed by deposition of titanium (Ti) and Au. The Ti layer is used to obtain good adhesion between the Nb underneath and the Au contact on top. To perform this deposition, an electron beam PVD tool is used. A schematic of this tool is given in Fig. 3.4. The target material is placed at the anode of a high voltage source, and is bombarded with an electron beam emitted from a high vacuum charged tungsten source. The atoms of the target are transformed into a gaseous phase and coat the entire chamber with a thin layer of the material. Once the layers are deposited, the wafer is placed in MICROPOSIT REMOVER 1165, which removes any resist left on the wafer and thus effectively lifting off the deposited layers where there was resist underneath.

3.3.3 Etching of the waveguide

To etch the Nb layer, only a single layer of imaging resist is needed. The resist is again spun on the wafer and baked. The exposure is again done with a laser writer. After exposure, the wafer is developed. The wafer is also plasma ashed with oxygen plasma. This is to remove any unwanted photoresist from the wafer surface that did not develop well. A plasma etch tool is used for this process, which uses monoatomic reactive species such as oxygen or fluorine. The plasma effectively creates ash from the photoresist, which is suctioned off through a vacuum pump. When ashing for a short duration, the term ‘descumming’ can be used, as only scum on the surface is removed. When ashing for a longer duration and with a higher power, the term ‘stripping’ is preferred, as a full layer is stripped from the surface. The Nb is then etched with reactive ion etching (RIE).

For the thesis work, two etching gasses were used: nitrogen trifluoride (NF_3) and sulfur hexafluoride (SF_6). The etching duration is also varied between some samples, either etching until the substrate is reached, or etching about twice that time to effectively etch into the substrate. Substrate detection is done by using a laser and measuring the reflection at a point on the wafer where the metal is being etched. Like this, a sudden change in the reflection indicates that the metal layer is fully etched away and the substrate is reached. As mentioned in Sec. 3.2, this reflection change is very pronounced when working with a sapphire substrate, in contrast to a more subtle change with silicon substrates.

Over etching

With two samples, we tried over etching the waveguide so that we etched into the substrate, which should help reduce TLS losses (Fig. 3.5) as we’re effectively moving an interface where TLS reside further away.

Some atomic force microscopy (AFM) measurements were done to investigate the surfaces of both the substrate and the waveguide to make sure the etching did not damage it, and to measure the depth of the etch into the substrate. The measured roughnesses are given in Table 3.2, and the measured depths are shown in Fig. 3.6.

During the measurements of both SF_6 samples, it was immediately clear that the surfaces of both the Nb and Si substrate were very rough (Fig. 3.6c). This roughness has a similar profile to leftover resist, leading us to believe that for the Nb surface, the extensive etching heated up the sample enough to burn the resist to the surface. For the Si substrate surface, we think that the etching damaged the surface, rather than it being left-over resist, since those areas were not covered by resist during the etch. By performing more extensive cleaning and performing another AFM measurement on the over etched sample, these explanations seem most likely, as the Nb surface is now less rough, while the Si surface does not seem to have changed (Fig. 3.6d).

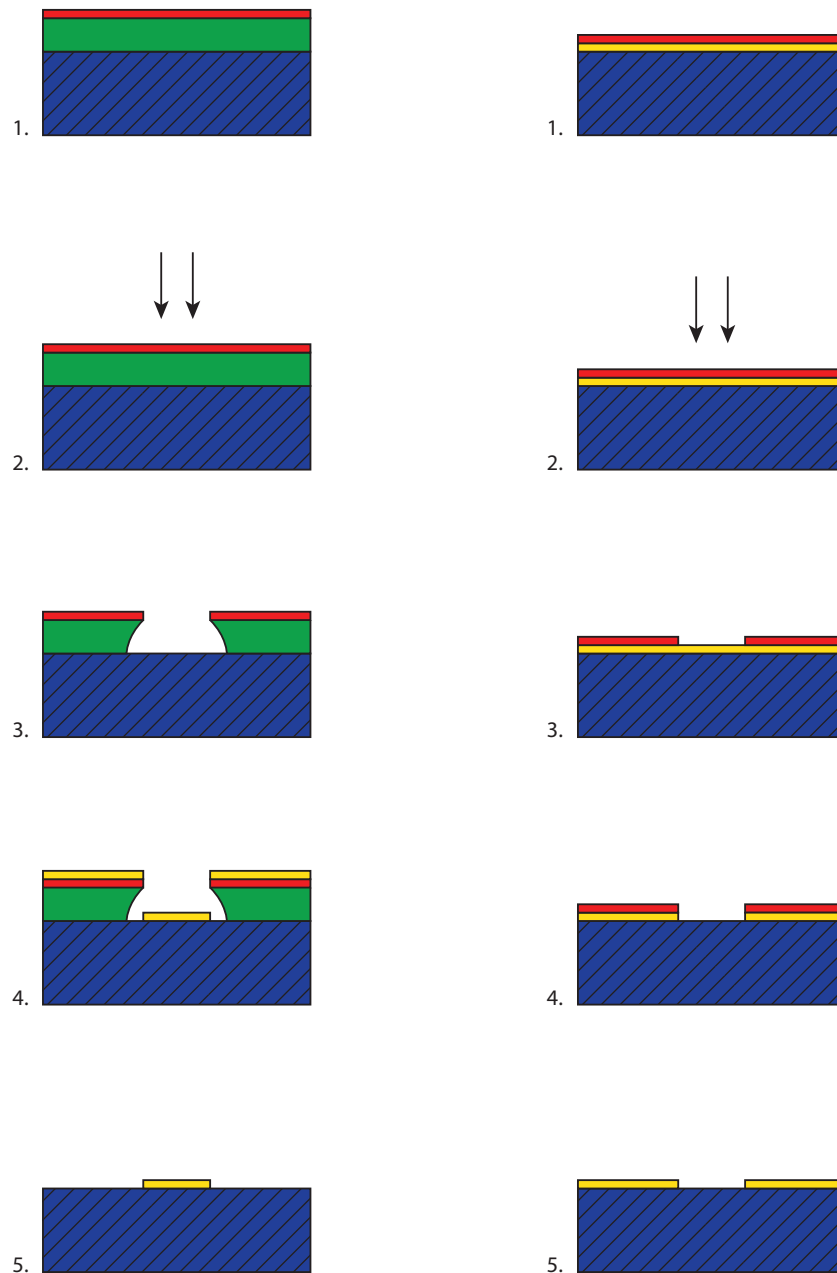


Figure 3.3: Photolithography processes used in the thesis work. Left: lift-off process. Lift-off resist (green) and photoresist (red) are spin-coated on a wafer (blue) (1). The resist is then exposed with a laser writer (2) and developed (3). A metal layer (yellow) is then deposited on top (4). After the wafer is placed in remover, metal remains only where the resist was originally exposed (5). Right: etching process. Photoresist is spin-coated on a wafer covered with a metal layer (1), the resist is then exposed with a laser writer (2). After development, only the unexposed resist remains (3). The uncovered metal is then removed in an etching step (4). Finally, the remaining resist is removed and metal remains in the unexposed area (5). Reprinted and modified with permission from [16].

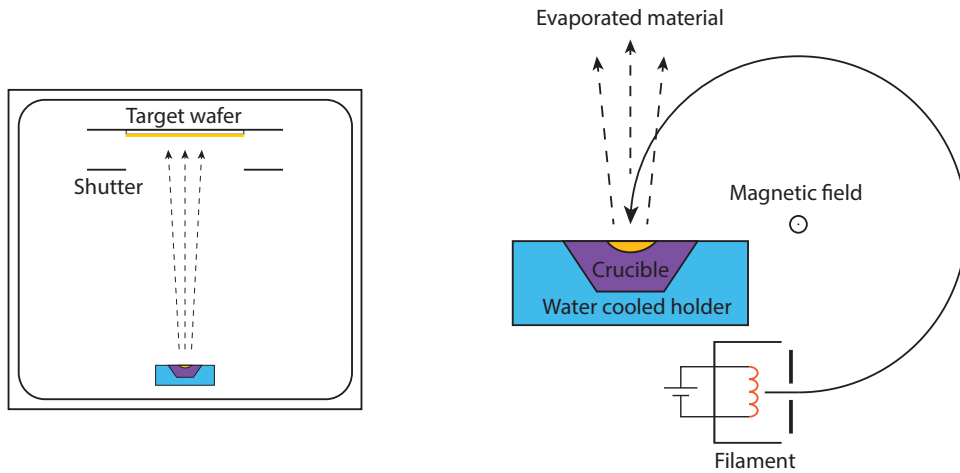


Figure 3.4: (Left) The target wafer is placed in a high-vacuum chamber. Once the material starts evaporating from the source, the shutter is opened and the material starts depositing on the target wafer. (Right) Detailed view of the source. The electrons emitted from the filament are directed by a magnetic field towards a water-cooled crucible filled with the desired material. The material heats up in contact with the electrons and evaporates. Reprinted with permission from [16].

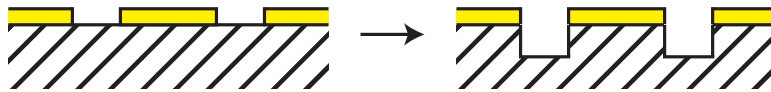
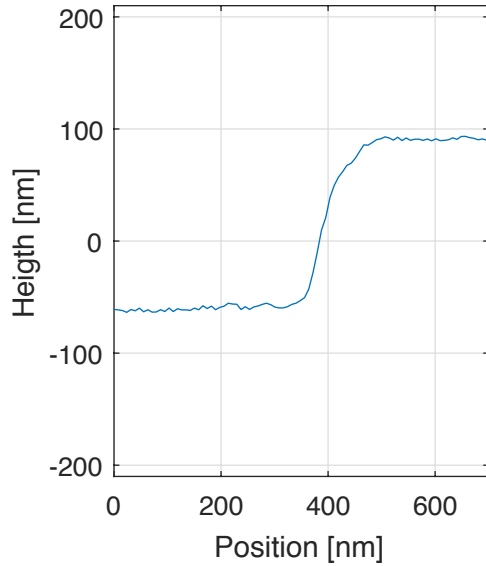


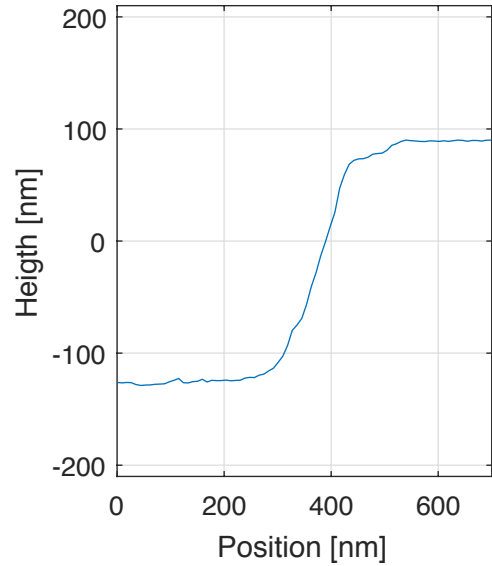
Figure 3.5: Schematic of over etching of the superconductor (yellow), in order to etch into the substrate (hashed).

Table 3.2: Measured roughness values of the surfaces of the superconductor and substrate for the two etching gasses and etching durations. R_a is the mean roughness, or roughness average, R_q is the root mean square (RMS) roughness, and R_{max} is the maximum roughness depth.

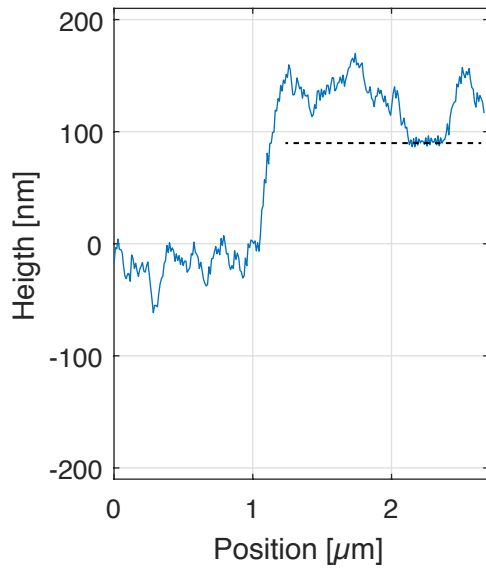
Etch gas	Etch depth [nm]	Superconductor			Substrate		
		R_a [nm]	R_q [nm]	R_{max} [nm]	R_a [nm]	R_q [nm]	R_{max} [nm]
NF ₃	150	3.13	4.16	29.4	1.17	1.53	32.9
	215	0.921	1.83	28.0	0.765	0.969	9.00
SF ₆	105	20.4	23.6	118	9.41	12.5	136
	253	10.6	13.3	108	22.6	28.0	159



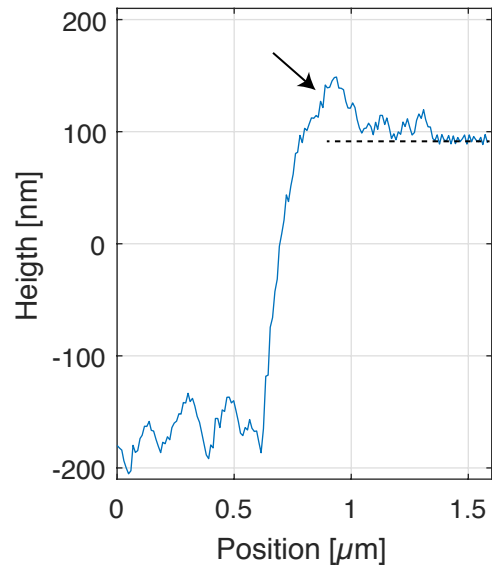
(a) NF_3 , normal etch.



(b) NF_3 , over etch.



(c) SF_6 , normal etch. A dashed line is added where the Nb surface is assumed to be, considering the flat region at the right.



(d) SF_6 , over etch. A dashed line is added where the Nb surface is. The arrow points to a typical phenomenon that resist tends to accumulate at the edge of the etch.

Figure 3.6: Profile section cuts of the two different etching gasses, and the two different etching durations. In each graph, the high plateau on the right is the superconductor and the low plateau on the left is the substrate underneath. The graphs are vertically offset so that the Nb-Si interface is at 0 nm height.

3.4 Cryogenic measurements

3.4.1 Cryostat

Since we are working with superconductors, we need to perform measurements in a low-noise environment. This means we need to work at temperatures well below the critical temperature of the superconductor, $T \ll T_c$. To this end, we use a helium-3 (^3He)/helium-4 (^4He) cryogen-free dilution refrigerator with a base temperature $T < 10$ mK.

In contrast to refrigerators using liquid nitrogen, the primary cooling in a cryogen-free refrigerator is provided by a pulse tube cryocooler. The working principle is based on the adiabatic compression and expansion of ^4He . The pulse tube cryocooler can reach a temperature of about 3 K.

The secondary cooling is based on the phase separation of a $^3\text{He}/^4\text{He}$ mixture that occurs when cooled down below 0.7 K. The phase separation divides the mixture in a concentrated, nearly pure ^3He phase and a dilute phase of ^3He and ^4He . By constantly removing ^3He from the dilute phase, ^3He will ‘evaporate’ from the concentrated phase to the dilute phase. This crossing of the phase boundary is what provides the cooling power to reach a base temperature $T < 10$ mK.

Several components in this type of cryostat have stable working temperatures. By attaching plates to these components, there are several temperature stages through which the measurement lines are fed, allowing for thermalisation of the lines and attenuation in several steps. The thermalisation is necessary due to the limited cooling power of the cryostat. Additionally, the measurement lines are chosen to have poor thermal conductivity. The attenuation along the lines is done to reduce noise coming from room temperature, as well as reducing the power level to the desired power regime.

3.4.2 Setup

The samples are wire bonded in a sample box before mounting it in the cryostat. The sample box has K connectors on the outside, which are connected with glass beads to the inside of the box. On the inside of the box, microstrips connect the glass beads to centre conductors on a printed circuit board (PCB) covering the entire inside of the box. The contacts of the sample are wire bonded to these conductors, while the ground plane of the sample is wire bonded to the ground plane of the PCB. In the middle of the PCB, a hole the size of the sample is cut out. This is where the sample is glued to the sample box, allowing for thermalisation through the bottom of the box to the cryostat.

To measure the sample, a vector network analyser (VNA) was used. With the VNA, the complex reflection and transmission response can be measured. As the output power range of the VNA spans 34 dBm (-27 dBm to 7 dBm), but we wanted to measure over a range of about 90 dBm, we had to measure in three runs with additional room temperature attenuators (no, one or two 30 dB attenuators). This 90 dBm power range, combined with a total of 60 dB attenuation in the cryostat and about 10 dB attenuation in the cables, feedthroughs, and connectors, translates into a range of roughly 1×10^{-2} photons to 1×10^7 photons in the resonators. The response is then amplified in two stages, with first a high electron mobility transistor (HEMT) amplifier of about 35 dB at the 4 K stage of the cryostat, and secondly a 24 dB amplifier at room temperature.

A detailed schematic of the setup in the cryostat is given in Fig. 3.7, where the signal follows these steps:

1. The incoming signal is attenuated while traversing the different cooling stages, as to reduce the thermal noise in the signal.
2. The signal passes through a low-pass and high-pass filter, with similar cut-off frequencies as the amplifier later in the setup.

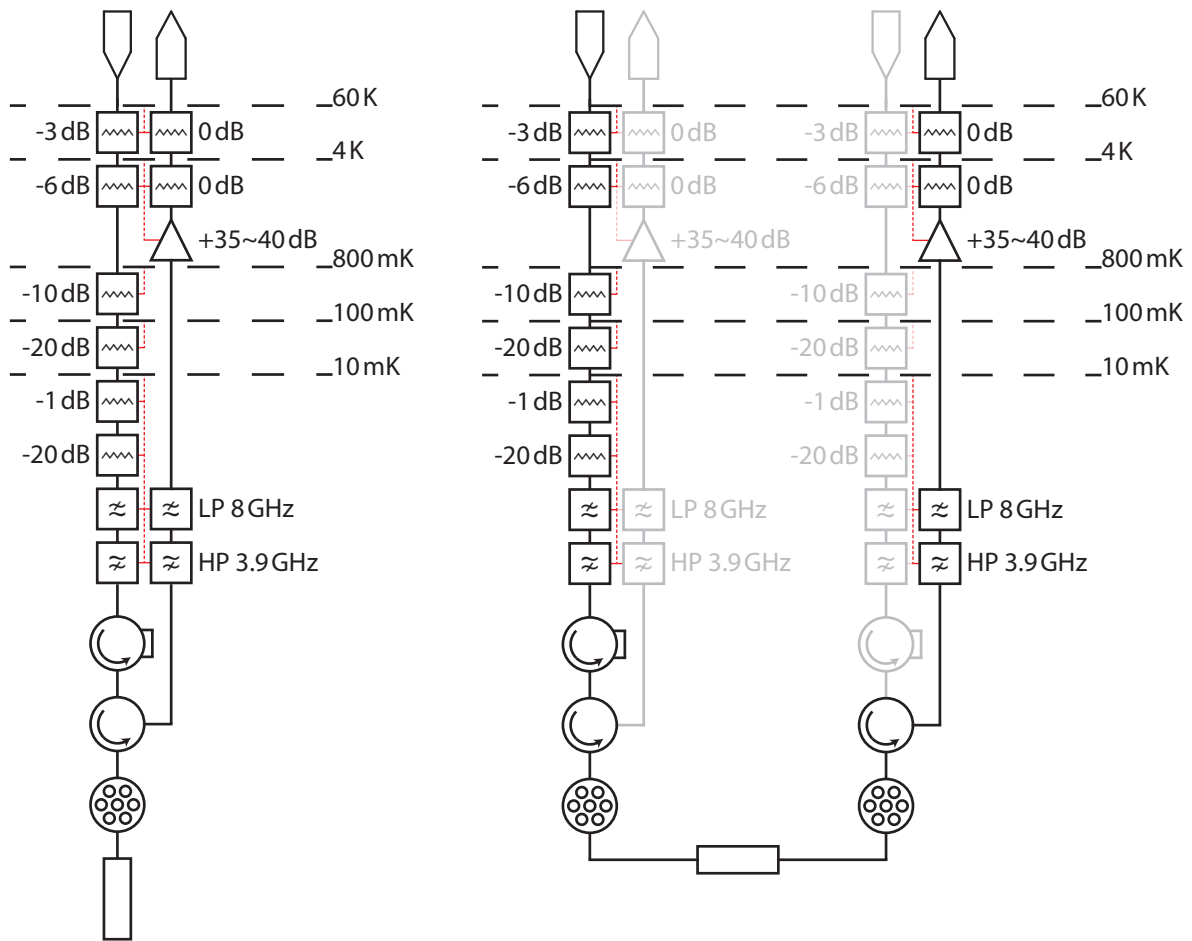


Figure 3.7: Schematic of the measurement setup for a reflection (left) or transmission (right) measurement. Red lines indicate the thermal grounding, and elements in grey are connected, but not used.

3. The signal passes through two circulators, whose purpose is to separate incoming from reflected signal, and to avoid having noise sent out by the amplifier later in the setup to be picked up in the measurement.
4. The signal passes through a switch.
5. The signal reaches the sample and is reflected, and also transmitted in case of a two-port sample.
6. The signal reaches the circulator where it is sent along the second line.
7. The signal passes through a second set of low- and high-pass filters.
8. The signal is amplified with about 35 dB.
9. The signal leaves the cryostat.

Part 4

Results

4.1 Measurement and fitting flow

4.1.1 Measurements

For all measurements, a certain workflow was used. First, a wide frequency scan with a large number of points at a medium power level is done, in order to easily ‘find’ the resonators. This is because, as mentioned in Sec. 3.1.1, the resonance frequency is sensitive to the various fabrication steps. As the goal of this first measurement is only to determine the resonance frequencies of the resonators, and thus looking at only the magnitude of the response is sufficient. Such a measurement is shown in Fig. 4.1 where the sharp vertical lines are the transmission dips caused by the resonators.

Next, each resonator is measured separately with more precision (typically a span of 6 MHz around the resonance frequency) to further refine the resonance frequency and to make sure that the full resonance is captured with the chosen span.

With the frequency window set up properly, power sweep measurements are the next step. Due to the limited output power range of the VNA (-27 dBm to 7 dBm), the full power sweep measurement is divided in three parts of 30 dBm, with no, one, or two additional -30 dB attenuators at the output of the VNA, giving a total range of 90 dBm. Aside from the extra attenuators, the three measurements have only one setting that does not stay constant, which is the amount of averaging. In order to reduce the noise at the lower power regime, up to almost ten times more averaging is done compared to the high power measurements.

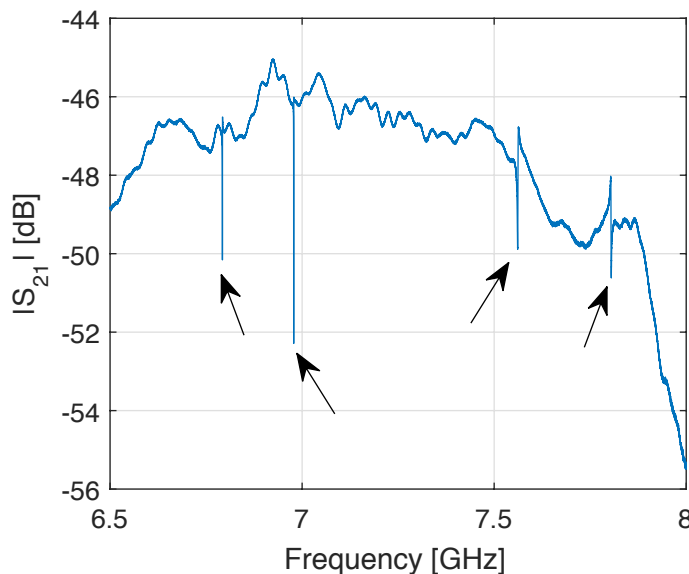


Figure 4.1: A wide frequency measurement of a sample in order to determine the resonance frequencies of the resonators (indicated with arrows).

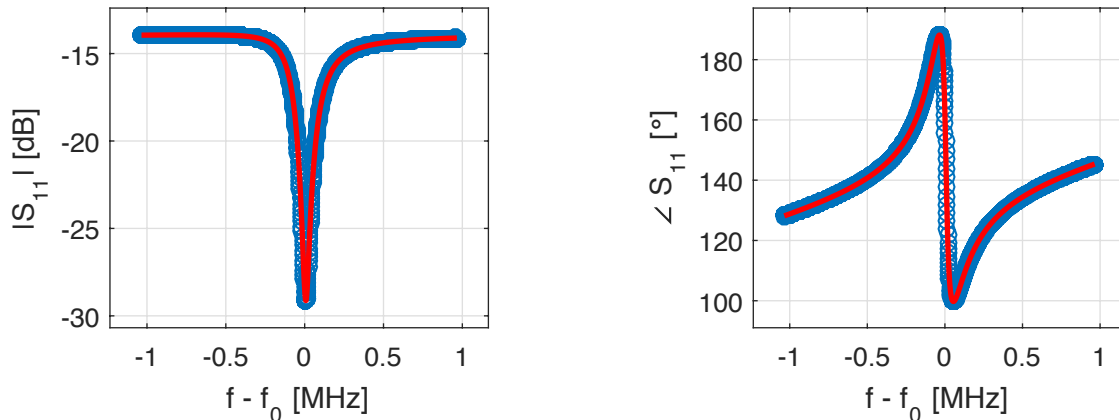


Figure 4.2: *Magnitude (left) and phase (right) response and the corresponding fit (red) at a high power.*

4.1.2 Fitting

Once the measurements have completed, the data is fed through a script that fits the data to the fitting function that was established in Sec. 2.1. The fitted parameters can be divided in two parts: four parameters are directly related to the resonator (f_0 , Q_i and the complex valued Q_e), and four parameters for first-order approximations of both the magnitude and phase background. The fitting is done using a non-linear least squares method.

Example

To show that the fit agrees well with the data, we will show detailed results from the first sample in this section. This particular resonator had a reflection setup.

In Fig. 4.2 the amplitude and phase of both the data and the fit are shown for the highest-power data. In the phase response, an approximated linear background is already subtracted to remove most of the effect of electrical delay according to Eq. (2.5), only fitting the frequency dependent angle ϕ_f . Without this, one would only see a straight line, spanning multiples of 360° . This figure already shows that the model closely fits the actual data.

To more closely resemble Fig. 2.4, the background can be subtracted from these figures using Eq. (2.4) and (2.5), resulting in Fig. 4.3. The magnitude is now at unity (or 0 dB) away from resonance, while the phase now has its shift around 0° , and no longer has the clear linearly increasing background. The linear background of the magnitude response is also subtracted, however this was very small for this resonator, and the effect is not visible in these figures.

Even at lower powers, the model fits the data accurately. However, due to noise on the signal, the extracted fit parameters will have larger uncertainty, or the fit may occasionally even simply fail. The data and the fit at a single photon power level is shown in Fig. 4.4 to show this.

One can then plot the fitted value for Q_i against the power level (Fig. 4.5) or look at the losses $\delta_i = 1/Q_i$ and fit Eq. (2.8) (Fig. 4.6). This power level is the power inside the resonator, and is not equal to the input power [3]. We can calculate the absorbed power in the resonator P_r with:

$$P_r = \frac{2Q_l^2}{Q_c Q_i} P_{in}$$

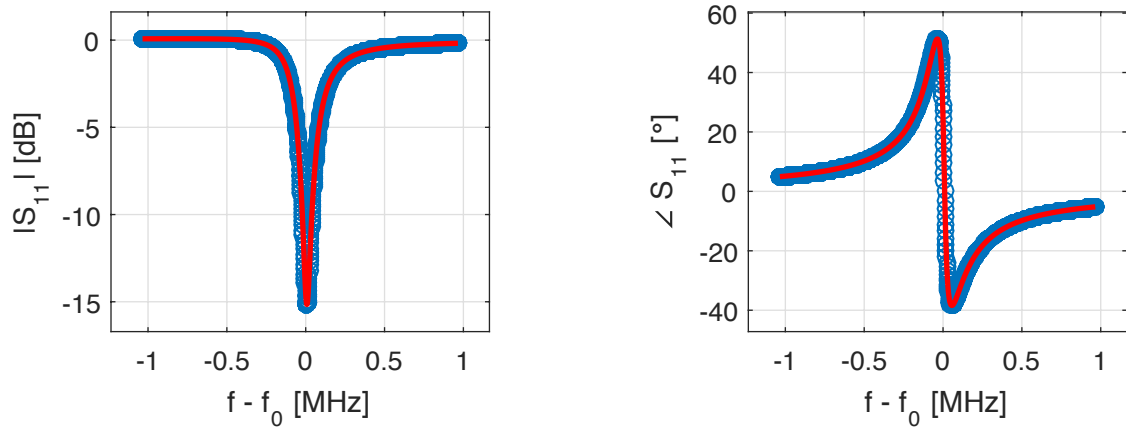


Figure 4.3: Magnitude (left) and phase (right) response and the corresponding fit (red) at a high power, with background subtraction.

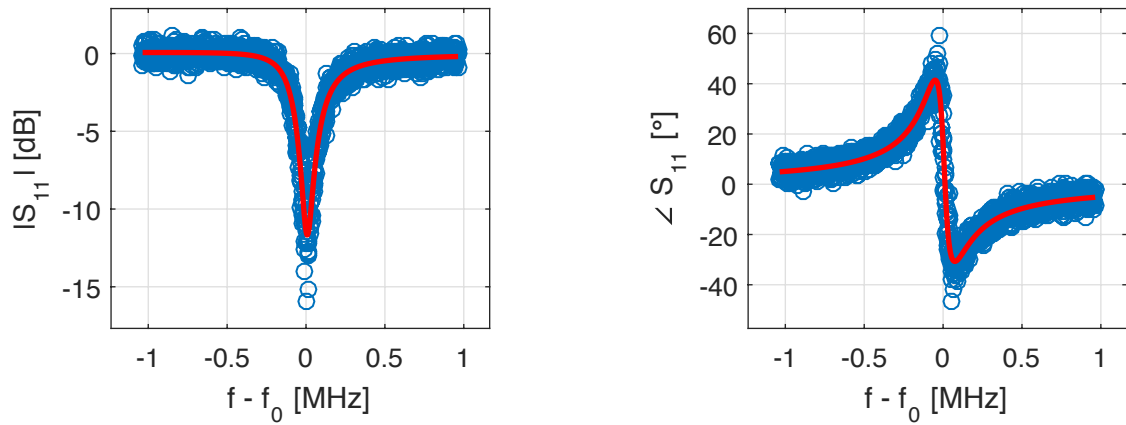


Figure 4.4: Magnitude (left) and phase (right) response and the corresponding fit (red) at the single photon power regime.

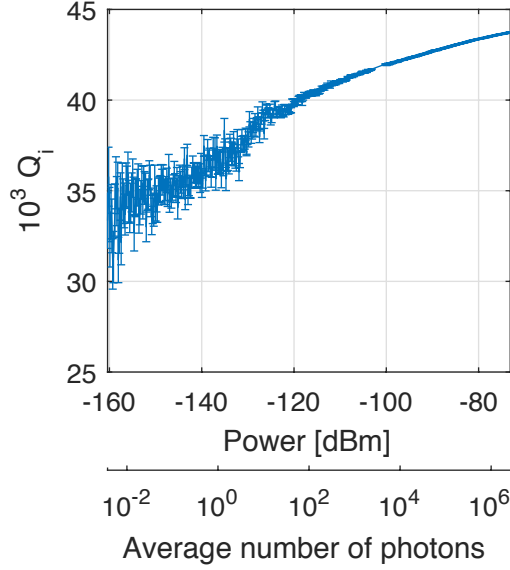


Figure 4.5: *Fitted value with confidence intervals for the internal quality factor Q_i in function of the power in the resonator.*

where P_{in} is the incident power. From this equation, we can see that at critical coupling, the absorbed power P_r will be equal to the incident power P_{in} . By then relating the stored energy E_r in the resonator to that power with

$$E_r = \frac{P_r}{\kappa_i},$$

where $\kappa_i = \omega_r/Q_i$ is the internal loss rate, we can calculate the average number of photons $\langle n \rangle$ by the energy per photon $E_{ph} = \hbar\omega_r$:

$$\begin{aligned} \langle n \rangle &= \frac{E_r}{\hbar\omega_r} \\ &= \frac{1}{\hbar\omega_r} \frac{P_r}{\kappa_i} \\ &= \frac{Q_i}{\hbar\omega_r^2} P_r \\ &= \frac{2Q_l^2}{\hbar\omega_r^2 Q_c} P_{in}. \end{aligned}$$

When looking at the coupling quality factor Q_c , which we calculate with Eq. (2.3), we would expect a constant value when plotting against power. While this was the case for most of the measured resonators (Fig. 4.7a), for some resonators there was a distinct power-dependent behaviour (Fig. 4.7b). While we do not have a physical explanation for this, we could also not see any correlation with other properties, e.g. the amount of asymmetry on the response.

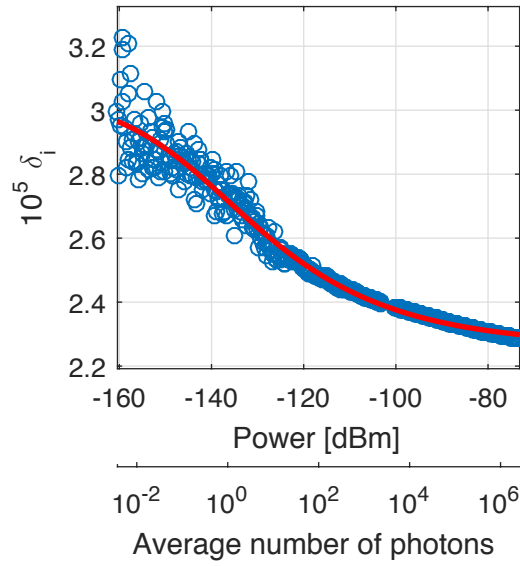


Figure 4.6: Losses $\delta_i = 1/Q_i$ in function of the power in the resonator and the fit to Eq. (2.8) (red).

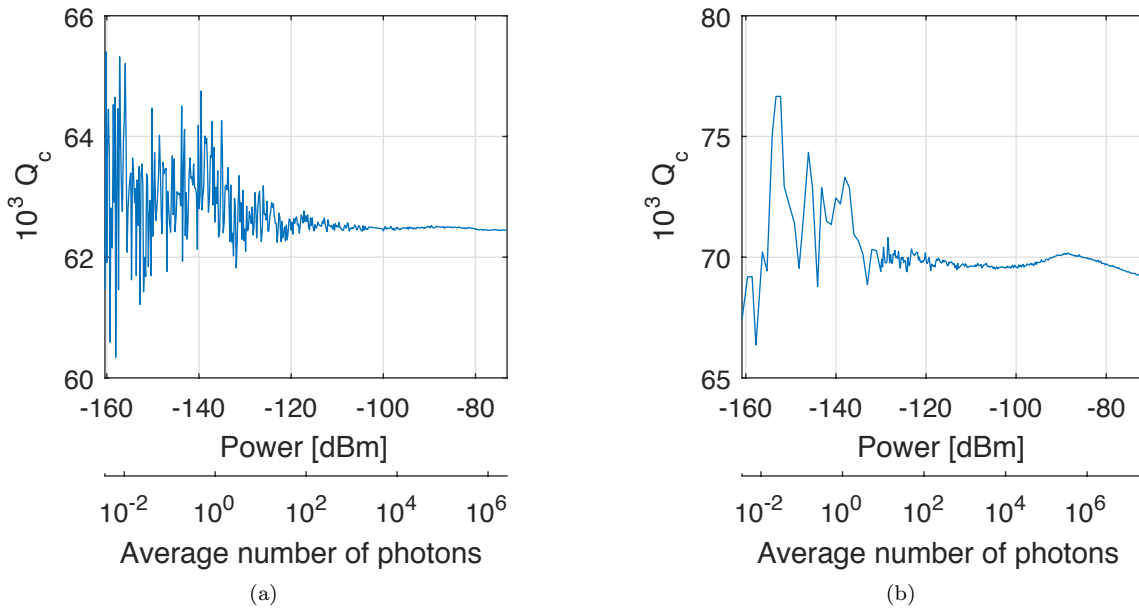


Figure 4.7: Coupling quality factor Q_c in function of the power in the resonator for two different resonators. At higher powers, the resonator on the left has a constant behaviour, as expected, while the one on the right shows a clear power dependency.

Table 4.1: An overview of all the samples. Three different design were used: SR01 is a single reflection resonator, MR01 consists of three resonators with three different centre line width and gap width combinations in a transmission setup, and MR02 consists of four resonators with two different centre line width and gap width combinations, and with a meandered and almost straight version, also in a transmission setup. Two different substrates were used, as well as two etching gasses. Over etching only happens with silicon substrates, of which the depth is measured with atomic force microscopy. The fitted value for the internal quality factor Q_i is given at a high power, 1×10^5 photons, and at a single photon level. Empty cells are were the fit did not resolve for the response.

Design	Substrate	Etch gas	Over etching [nm]	Centre line width [μm]	Gap width [μm]	Meandering	High power Q_i [1×10^3] (1×10^5 photons)	Single photon Q_i [1×10^3]	
SR01	sapphire	NF ₃	-	15	7	yes	42.9 ± 0.01 %	36.5 ± 1.7 %	
MR01	sapphire	NF ₃	-	10	5	yes	200 ± 0.4 %	64.6 ± 7.6 %	
				20	10	yes	28.6 ± 0.2 %	24.8 ± 2.6 %	
				25	12	yes	1.46 ± 0.2 %	1.46 ± 0.2 %	
				3	2	yes	51.6 ± 0.2 %	38.5 ± 3.5 %	
MR02	silicon	NF ₃	70	10	5	yes	6.23 ± 0.03 %	6.02 ± 0.7 %	
					no	12.8 ± 0.1 %	11.9 ± 1.7 %		
				125	3	2	yes	246 ± 0.2 %	84.3 ± 2.9 %
					no	442 ± 0.5 %	126 ± 7.9 %		
			20	10	5	yes	39.7 ± 0.06 %	34.7 ± 1.5 %	
					no	485 ± 0.1 %	295 ± 4.9 %		
				3	2	yes	174 ± 0.2 %	56.8 ± 5.3 %	
					no	38.4 ± 0.1 %	24.9 ± 4.0 %		
		170	10	5	yes	42.3 ± 0.09 %	34.4 ± 6.4 %		
				no	47.5 ± 0.04 %	37.6 ± 5.6 %			
			3	2	yes	199 ± 0.2 %	70.4 ± 8.2 %		
				no					
		10	5	yes	136 ± 0.03 %	72.2 ± 3.7 %			
			no	297 ± 0.07 %					

4.2 Results and discussion

4.2.1 Sample overview

A full overview of the different resonators that were measured are given in Table 3.1. The table includes information about the geometry (widths of centre conductor and gap, meandering) and etching (etching gas and amount of etching into the substrate). The extracted internal quality factors Q_i at high power (1×10^5 photons) and at single photon level are also included.

As can be seen in the table, confidence intervals at high power are small with regards to the value. Therefore, those confidence intervals will be omitted in figures in this section for clarity and to avoid confusion.

4.2.2 Centre conductor and gap width

By changing the centre line conductor and gap widths and making them smaller, we expected to reduce radiation losses and magnetic vortex losses. As can be seen in Fig. 4.8, there is indeed a trend in the fit results for the internal quality factor Q_i , that the quality increases – and thus the losses reduce – by going to smaller widths.

The choice to plot against $W + S$ is based on the dependence of the radiation losses on $W + S$, see Eq. (2.7) [1, 10]. Additionally, that implies that we could fit an equation to the internal quality:

$$Q_i^{-1} = \frac{1}{Q_0} + \frac{(W + S)^n}{\alpha},$$

where $n \approx 2$, and Q_0 and α are fit parameters. However, because of our limited dataset, this was not something we tried.

There are resonators that do not agree with that trend, but one needs to keep in mind that during the timeframe of the thesis work, we could not fabricate and measure multiple identical resonators to also look at the reproducibility of the results. It is thus better to assume that those specific resonators are performing worse than expected, e.g. due to sample box resonances, or fabrication issues.

4.2.3 Meandering

While not sure what effect it would have, we tried meandered and not meandered structures. From the comparison in Fig. 4.9, there seems to be a trend that meandering has a negative effect on Q_i . This probably originates from some inductive and capacitive coupling between the meandered lines.

When looking at the fit results for the power-dependent and -independent loss terms $\delta_{0,TLS}$ and δ_c , the improvement seems to originate from power-independent factors, rather than the power-dependent TLS losses.

4.2.4 Etching

In Fig. 4.11, a comparison of high power internal quality factor Q_i is given with respect to the different etching gasses that were used. From the figure, one can see that there is no particular correlation.

However, when looking at the effect of etching into the substrate, a clear increase in the high-power Q_i when performing this over-etch is noticeable (Fig. 4.12). As discussed in Sec. 3.3.3, the over etching

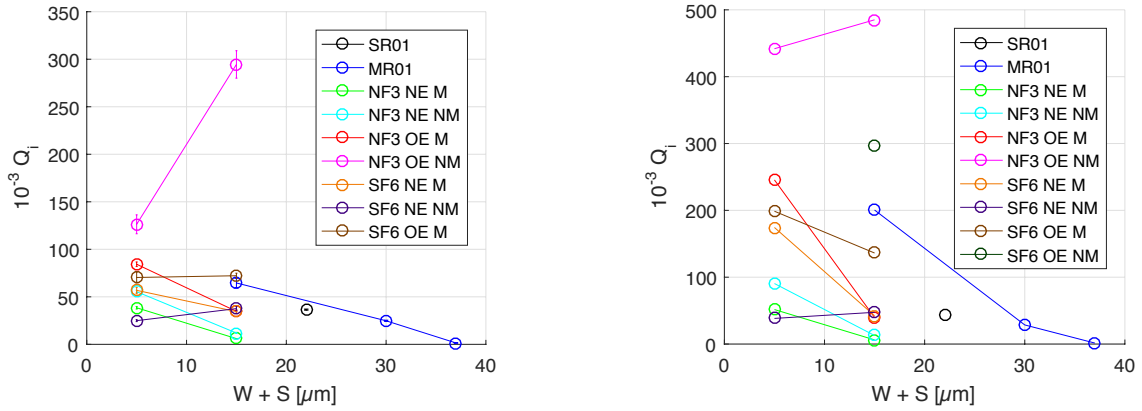


Figure 4.8: Comparison of Q -factor with respect to the sum of centre conductor width W and gap width S . Left: single photon Q_i . Right: high power Q_i , 1×10^5 photons. Abbreviations used in the legend: ‘SR01’ and ‘MR01’ are samples with one reflection resonator and three transmission resonators, respectively, ‘NF3’ and ‘SF6’ for the two used etching gasses, ‘NE’ and ‘OE’ for normal etching and over-etching, and ‘M’ and ‘NM’ for meandered and not meandered.

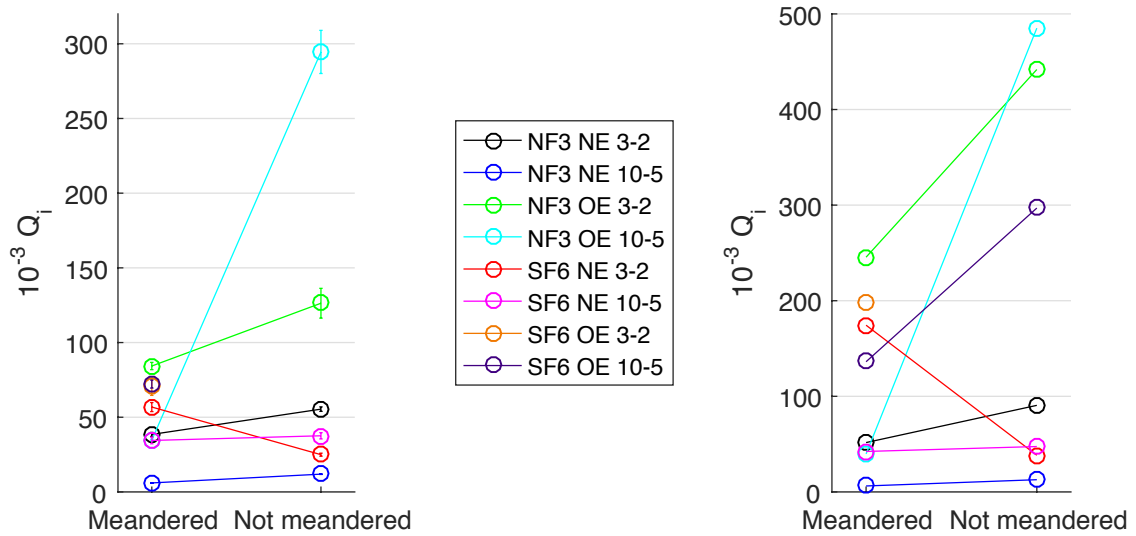


Figure 4.9: Comparison of internal Q -factor with respect to whether or not the resonators were meandered. Left: single photon Q_i . Right: high power Q_i , 1×10^5 photons. Abbreviations used in the legend: ‘NF3’ and ‘SF6’ for the two used etching gasses, ‘NE’ and ‘OE’ for normal etching and over-etching, and ‘3-2’ and ‘10-5’ for the different combinations of centre conductor and gap width.

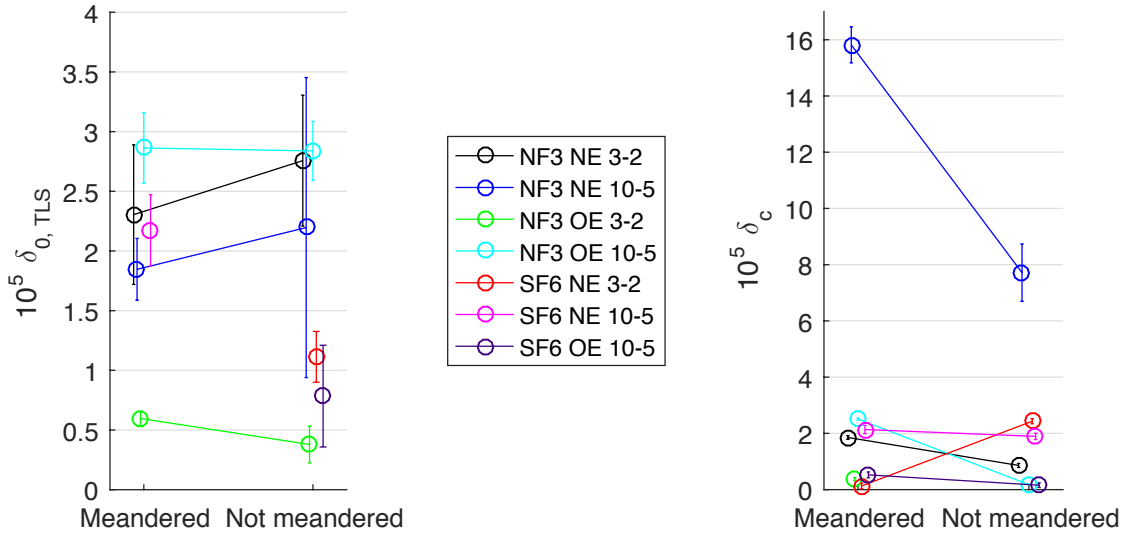


Figure 4.10: Comparison of fit values $\delta_{0, TLS}$ (left) and δ_c (right) with respect to whether or not the resonators were meandered. The individual data points and corresponding error bars are slightly horizontally offset for clarity. Abbreviations used in the legend: ‘NF3’ and ‘SF6’ for the two used etching gasses, ‘NE’ and ‘OE’ for normal etching and over-etching, and ‘3-2’ and ‘10-5’ for the different combinations of centre conductor and gap width.

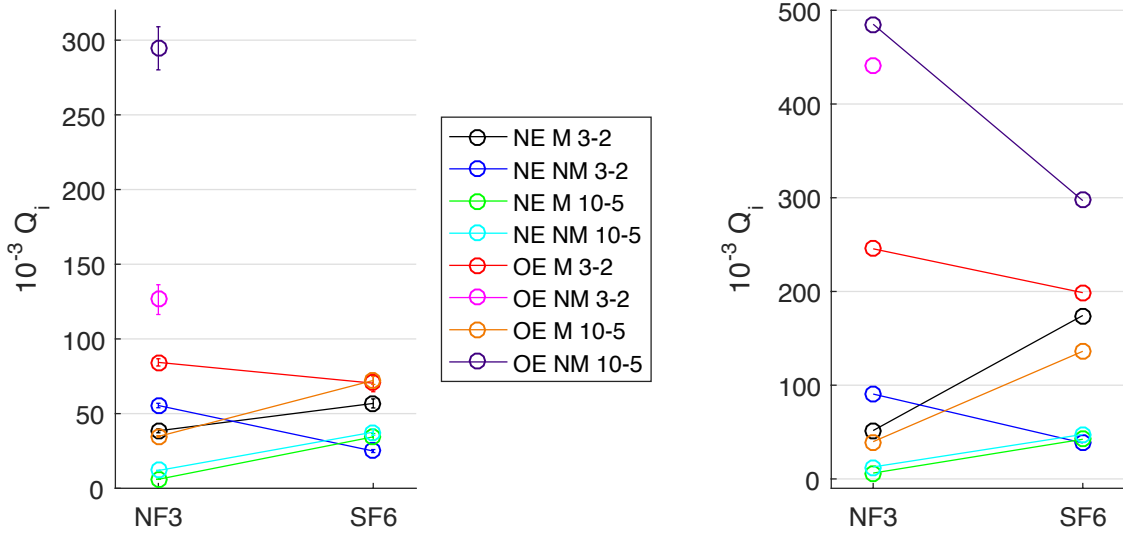


Figure 4.11: Comparison of internal Q-factor with respect to the two different etching gasses. Left: single photon Q_i . Right: high power Q_i , 1×10^5 photons. Abbreviations used in the legend: ‘NE’ and ‘OE’ for normal etching and over-etching, ‘M’ and ‘NM’ for meandered and not meandered, and ‘3-2’ and ‘10-5’ for the different combinations of centre conductor and gap width.

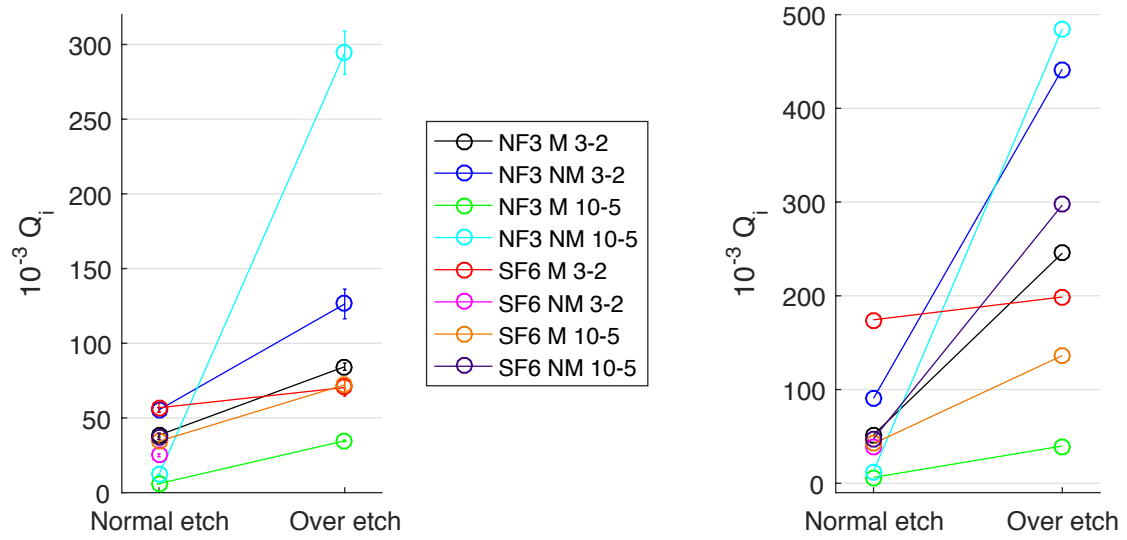


Figure 4.12: Comparison of internal Q -factor with respect to whether or not there was etching into the substrate. Left: single photon Q_i . Right: high power Q_i , 1×10^5 photons. Abbreviations used in the legend: ‘NF3’ and ‘SF6’ for the two used etching gasses, ‘M’ and ‘NM’ for meandered and not meandered, and ‘3-2’ and ‘10-5’ for the different combinations of centre conductor and gap width.

should reduce TLS losses. And indeed, fit results seem to show that TLS losses are reduced consistently, as well as the power-independent losses (Fig. 4.13).

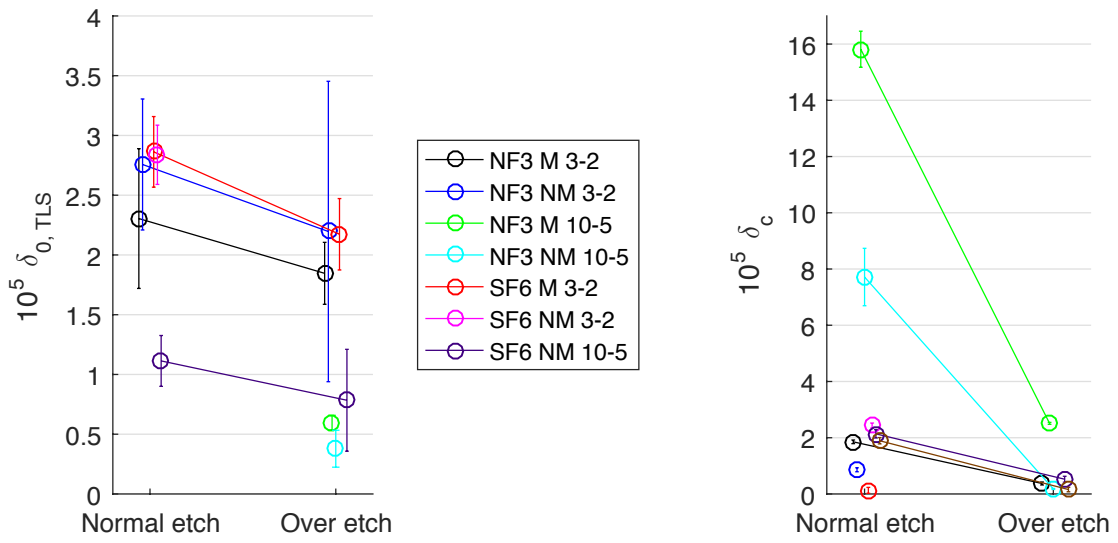


Figure 4.13: Comparison of fit values $\delta_{0, TLS}$ (left) and δ_c (right) with respect to whether or not there was etching into the substrate. Abbreviations used in the legend: ‘NF3’ and ‘SF6’ for the two used etching gasses, ‘M’ and ‘NM’ for meandered and not meandered, and ‘3-2’ and ‘10-5’ for the different combinations of centre conductor and gap width.

Part 5

Conclusion

During this thesis work, we studied a way to characterise resonators and their internal quality by fitting their signal response. The main expected mechanisms of losses were discussed, together with a means of reducing them. Then the design was discussed in more detail, as well as the parameters that were varied in order to reduce the losses that were seen earlier. The fabrication of the samples was shown and the varied parameters here were discussed, together with some discussion on the results of the fabrication. Next, the measurement setup and flow have been described. In the final part, we investigated the numerical results of the fits to the measurement data. We compared results for the different varied parameters and how these align with expectations and theory.

The results give a guideline to researchers how to improve resonator and possibly the full device quality by making some changes to the design and fabrication. However, there are more points to research to further improve resonators. Firstly, some points with regards to design:

Narrower widths We have shown that making resonators more narrow improves their quality. While we were limited during this work by the resolution of photolithography, by using other tools, like electron beam lithography (EBL) with a resolution of about 10 nm, one could easily make smaller resonators. However, we suspect that there will be an optimal width, where other effects will take dominance and reduce quality when trying to reduce the width even further (e.g. critical current). To find that optimal point in dimensions is one point for future research.

Meandering While meandering can only be avoided when having sufficient sample area, one could investigate the nature of that dependence more thoroughly. Additionally, one could also investigate whether the spacing between meanders can be optimised to where you can still have meandered resonators, but avoid the negative effects.

Resonance frequency As Eq. (2.7) shows, losses scale with the resonance frequency. Studying the significance of this effect within the measurement window (4 GHz to 8 GHz) is another point of interest.

Vortex pinning holes To avoid the dissipative motion of trapped magnetic vortices, holes could be added in the superconducting layer that would pin the vortices.

Secondly, with regards to the fabrication of the resonators we have:

Etch process As was shown, the used etch process (for SF₆, as well as for NF₃) can be optimised to reduce the surface roughness and better control the etch depth.

Etch depth Clearly, etching into the substrate improves the quality of the resonators. We speculate that there will be a point in depth where additional etching will have minimal incremental benefit. To find that depth is another point of interest.

Superconducting layer thickness During this thesis work, we used a constant thickness of the superconducting layer (90 nm), but this is certainly a parameter that can be changed and studied.

Superconducting material and deposition Several studies have used different superconducting materials, as opposed to Nb, as well as different techniques of depositing the superconducting layer, such as epitaxially growing the layer, for comparing the quality and have shown higher quality factors with e.g. aluminium, rhenium and titanium nitride, and epitaxially grown Nb in comparison to sputtered Nb [1].

The list of possible future research in improving resonators is of course not limited to this list.

Appendices

A Recipes

A.1 Wafer cleaning

A.1.1 Sapphire wafer

1. Place in a bath of MICROPOSIT REMOVER 1165 at 80 °C for 5 min.
2. Place in an ultrasonic bath for 1 min.
3. Place in a bath of propan-2-ol (isopropyl alcohol, IPA) for 2 min.
4. Perform a quick dump rinse (QDR).
5. Blow dry.
6. Plasma strip with 40 sccm O₂ at 500 mTorr and a power of 250 W for 1 min.

A.1.2 Silicon wafer

1. Place in an ultrasonic bath for 1 min.
2. Place in a bath of IPA for 2 min.
3. Blow dry.
4. Plasma strip with 40 sccm O₂ at 500 mTorr and a power of 350 W for 1 min.
5. Dip in a hydrofluoric acid (HF) bath for 10 s.
6. Blow dry.

A.2 Lift-off

1. Bake at 110 °C for 1 min.
2. Spin lift-off resist LOR 3B at 3000 rpm for 1 min with an acceleration time of 1.5 s.
3. Bake at 200 °C for 5 min.
4. Spin imaging resist S1813 at 3000 rpm for 1 min with an acceleration time of 1.5 s.
5. Bake at 110 °C for 2 min.
6. Expose with the mask aligner.
7. Develop using MF319 during 45 s.
8. Blow dry.
9. Plasma descum with 15 sccm O₂ at 250 mTorr and a power of 50 W for 20 s.

10. Deposit metal layer(s).
11. Perform lift-off with a bath of MICROPOSIT REMOVER 1165 at 80 °C for 5 min and at room temperature for 1 h.
12. Place in a bath of IPA for 1 min.
13. Perform a QDR.
14. Blow dry.

A.3 Etching

1. Bake at 115 °C for 2 min.
2. Spin imaging resist S1805 at 3000 rpm for 1 min with an acceleration time of 1.5 s.
3. Bake at 115 °C for 2 min.
4. Expose with the laser writer.
5. Develop using MICROPOSIT MF CD-26 during 45 s.
6. Perform a QDR.
7. Blow dry.
8. Etch using
 - NF₃** for 45 s to 60 s, or 90 s for an over etch, using 50 sccm NF₃.
 - SF₆** for 60 s, or 90 s for an over etch, using 100 sccm SF₆ and 40 sccm Ar.
9. 3 versions:
 - SR01
 - (a) Plasma descum with 15 sccm O₂ at 250 mTorr and a power of 50 W for 20 s.
 - (b) Place in a bath of MR-REM 400 for 1 min.
 - (c) Place in a bath of IPA for 1 min.
 - (d) Perform a QDR.
 - (e) Blow dry.
 - MR01
 - (a) Place in a bath of MICROPOSIT REMOVER 1165 at 80 °C for 5 min.
 - (b) Place in a bath of IPA for 1 min.
 - (c) Perform a QDR.
 - (d) Blow dry.
 - (e) Plasma descum with 15 sccm O₂ at 250 mTorr and a power of 50 W for 1 min.
 - MR02
 - (a) Plasma strip with 40 sccm O₂ at 500 mTorr and a power of 250 W for 1 min.
 - (b) Place in a bath of MR-REM 400 for 1 min.
 - (c) Place in a bath of IPA for 1 min.
 - (d) Perform a QDR.
 - (e) Blow dry.

A.4 Dicing

1. Bake at 120 °C for 1.5 min.
2. Spin protective resist S1813 at 3000 rpm for 1 min with an acceleration time of 1.5 s.
3. Bake at 115 °C for 2 min.
4. Dice.
5. Place in a bath of MICROPOSIT REMOVER 1165 at 80 °C for 5 min.
6. Place in a bath of IPA for 1 min.
7. Clean with water.
8. Blow dry.
9. (Plasma descum with 15 sccm O₂ at 250 mTorr and a power of 50 W/100 W for 1 min.)

B Transmission Fitting Function

There are multiple ways to derive a fitting function. In Section B.1, I derive a function in an analogous way to how the used reflection fitting function (Equation (2.1)) was derived, resulting in a similar form [4].

In Section B.2, another format is derived, starting from a different equation.

In Section B.3, a different end format is derived starting from the last intermediate step in Section B.2.

B.1 Analogous to the reflection fitting function

The transmission coefficient S_{21} is related to the input and output impedances Z_0 and the resonator impedance Z_R as

$$S_{21} = \frac{2Z_R}{Z_0 + 2Z_R} \quad (\text{B.1})$$

where the resonator impedance of the coupling capacitor and equivalent circuit of the coplanar waveguide is

$$Z_R = \frac{1}{i\omega C_C} + \left(\frac{1}{R_R} + \frac{1}{i\omega L_R} + i\omega C_R \right)^{-1} = \frac{1 - \omega^2 L_R (C_C + C_R) + i\omega \frac{L_R}{R_R}}{i\omega C_C (1 - \omega^2 L_R C_R) - \omega^2 C_C \frac{L_R}{R_R}}. \quad (\text{B.2})$$

Substitution of Equation (B.2) in Equation (B.1) gives

$$S_{21} = \frac{1 - \omega^2 L_R (C_R + C_C) + i\omega \frac{L_R}{R_R}}{1 - \omega^2 L_R \left(C_R + C_C \left(1 + \frac{Z_0}{2R_R} \right) \right) + i\omega \left(\frac{L_R}{R_R} + \frac{1}{2} Z_0 C_C (1 - \omega^2 L_R C_R) \right)}.$$

Substituting the resonance angular frequency $\omega_0 = 1/\sqrt{L_R(C_R + C_C)}$ and assuming that $R_R \gg Z_0$ gives

$$S_{21} = \frac{1 - \left(\frac{\omega}{\omega_0} \right)^2 + i \frac{\omega}{\omega_0} \omega_0 \frac{L_R}{R_R}}{1 - \left(\frac{\omega}{\omega_0} \right)^2 + i \frac{\omega}{\omega_0} \left(\omega_0 \frac{L_R}{R_R} + \frac{1}{2} \omega_0 Z_0 C_C \left(1 - \left(\frac{\omega}{\omega_0} \right)^2 \omega_0^2 L_R C_R \right) \right)}. \quad (\text{B.3})$$

By defining the internal quality factor Q_i and external quality factor Q_e as

$$Q_i = \omega_0 R_R (C_R + C_C)$$

$$Q_e = \frac{C_R + C_C}{\omega_0 Z_0 C_C^2}$$

we can substitute these into Equation (B.3):

$$S_{21} = \frac{1 - \left(\frac{\omega}{\omega_0} \right)^2 + i \frac{\omega}{\omega_0} \frac{1}{Q_i}}{1 - \left(\frac{\omega}{\omega_0} \right)^2 + i \frac{\omega}{\omega_0} \left(\frac{1}{Q_i} + \frac{C_R + C_C - \left(\frac{\omega}{\omega_0} \right)^2 C_R}{C_C Q_e} \right)}. \quad (\text{B.4})$$

Assuming small detuning from the resonance frequency, we can write

$$\omega = \omega_0 + \delta\omega$$

so that

$$\frac{\omega}{\omega_0} = 1 + \frac{\delta\omega}{\omega_0}$$

$$\left(\frac{\omega}{\omega_0}\right)^2 = 1 + 2\frac{\delta\omega}{\omega_0}$$

when ignoring higher orders of $\delta\omega$. Substituting this into Equation (B.4) and multiplying by $-\omega_0/2$ gives

$$S_{21} = \frac{\delta\omega - i\omega_0\frac{1}{2Q_i} - i\delta\omega\frac{1}{2Q_i}}{\delta\omega - i\left(\frac{\omega_0}{2Q_i} + \frac{\omega_0}{2Q_e} - \frac{C_R\delta\omega}{C_C Q_e}\right) - i\delta\omega\left(\frac{1}{2Q_i} + \frac{1}{2Q_e}\right)}$$

$$\approx \frac{\delta\omega - i\omega_0\frac{1}{2Q_i}}{\delta\omega - i\omega_0\left(\frac{1}{2Q_i} + \frac{1}{2Q_e}\right)}.$$

Finally, we divide by 2π and arrange the equation to

$$S_{21} = \frac{\delta f^2 + f_0^2\frac{1}{4Q_i}\left(\frac{1}{Q_i} + \frac{1}{Q_e}\right) + if_0\delta f\frac{1}{2Q_e}}{\delta f^2 + \frac{1}{4}f_0^2\left(\frac{1}{Q_i} + \frac{1}{Q_e}\right)^2}.$$

B.2 Alternative derivation

Instead of starting from Equation (B.1), one can also start from

$$S_{21} = 1 - \frac{Z_0}{2Z_R + Z_0}.$$

Substituting Equation (B.2) for the resonator impedance Z_R gives

$$S_{21} = 1 - \frac{\frac{1}{2}Z_0\left(i\omega C_C(1 - \omega^2 L_R C_R) - \omega^2 C_C\frac{L_R}{R_R}\right)}{1 - \omega^2 L_R(C_R + C_C) + i\omega\frac{L_R}{R_R} + \frac{1}{2}Z_0\left(i\omega C_C(1 - \omega^2 L_R C_R) - \omega^2 C_C\frac{L_R}{R_R}\right)}.$$

Substituting the resonance angular frequency $\omega_0 = 1/\sqrt{L_R(C_R + C_C)}$ and assuming that $R_R \gg Z_0$ gives

$$S_{21} = 1 - \frac{i\frac{\omega}{\omega_0}\omega_0 Z_0 C_C\left(1 - \left(\frac{\omega}{\omega_0}\right)^2 \omega_0^2 L_R C_R\right)}{1 - \left(\frac{\omega}{\omega_0}\right)^2 + i\frac{\omega}{\omega_0}\omega_0\left(\frac{L_R}{R_R} + Z_0 C_C\left(1 - \left(\frac{\omega}{\omega_0}\right)^2 \omega_0^2 L_R C_R\right)\right)}.$$

Substituting the internal quality factor Q_i and external quality factor Q_e gives

$$S_{21} = 1 - \frac{i\frac{\omega}{\omega_0}\frac{C_R + C_C - \left(\frac{\omega}{\omega_0}\right)^2 C_R}{C_C Q_e}}{1 - \left(\frac{\omega}{\omega_0}\right)^2 + i\frac{\omega}{\omega_0}\left(\frac{1}{Q_i} + \frac{C_R + C_C - \left(\frac{\omega}{\omega_0}\right)^2 C_R}{C_C Q_e}\right)}.$$

Assuming small detuning gives

$$\begin{aligned}
S_{21} &= 1 - \frac{i \frac{C_C - 2 \frac{\delta\omega}{\omega_0} C_R}{C_C Q_e} + i \frac{\delta\omega}{\omega_0} \frac{C_C - 2 \frac{\delta\omega}{\omega_0} C_R}{C_C Q_e}}{-2 \frac{\delta\omega}{\omega_0} + i \left(\frac{1}{Q_i} + \frac{1}{Q_e} - \frac{2\delta\omega C_R}{\omega_0 C_C Q_e} \right) + i \frac{\delta\omega}{\omega_0} \left(\frac{1}{Q_i} + \frac{1}{Q_e} - \frac{2\delta\omega C_R}{\omega_0 C_C Q_e} \right)} \\
&\approx 1 - \frac{\frac{1}{Q_e}}{2i \frac{\delta\omega}{\omega_0} + \left(\frac{1}{Q_i} + \frac{1}{Q_e} \right)}. \tag{B.5}
\end{aligned}$$

Introducing the loaded quality factor $Q_l^{-1} = Q_i^{-1} + Q_e^{-1}$, we can change the equation to

$$S_{21} = 1 - \frac{Q_l/Q_e}{1 + 2iQ_l \frac{\delta\omega}{\omega_0}}$$

which is a form used several times in literature [3, 5-7].

B.3 Alternative form

Starting with Equation (B.5), one can write the transmission as

$$S_{21}^{-1} = \frac{1}{1 - \frac{\frac{1}{Q_e}}{2i \frac{\delta\omega}{\omega_0} + \left(\frac{1}{Q_i} + \frac{1}{Q_e} \right)}}$$

which can then be simplified to

$$S_{21}^{-1} = 1 + \frac{Q_i}{Q_e} \frac{1}{1 + 2iQ_i \frac{\delta\omega}{\omega_0}}$$

which is another form used in literature [2].

References

- [1] J. M. Sage et al. ‘Study of loss in superconducting coplanar waveguide resonators’. *Journal of Applied Physics* 109.6 (2011), p. 063915.
- [2] A. Megrant et al. ‘Planar superconducting resonators with internal quality factors above one million’. *Applied Physics Letters* 100.11 (2012), pp. 1–4.
- [3] A. Bruno et al. ‘Reducing intrinsic loss in superconducting resonators by surface treatment and deep etching of silicon substrates’. *Applied Physics Letters* 106.18 (2015), p. 182601.
- [4] P. Krantz. ‘Parametrically pumped superconducting circuits’. MA thesis. Chalmers University of Technology, 2013.
- [5] D. P. Pappas et al. ‘Two level system loss in superconducting microwave resonators’. *IEEE Transactions on Applied Superconductivity* 21.3 PART 1 (2011), pp. 871–874.
- [6] M. S. Khalil, F. C. Wellstood and K. D. Osborn. ‘Loss dependence on geometry and applied power in superconducting coplanar resonators’. *IEEE Transactions on Applied Superconductivity* 21.3 PART 1 (2011), pp. 879–882.
- [7] M. S. Khalil et al. ‘An analysis method for asymmetric resonator transmission applied to superconducting devices’. *Journal of Applied Physics* 111.5 (2012).
- [8] J. Gao. ‘The Physics of Superconducting Microwave Resonators’. PhD thesis. California Institute of Technology, 2008.
- [9] J. Goetz et al. ‘Loss mechanisms in superconducting thin film microwave resonators’. *arXiv* 015304.May (2015), pp. 1–8.
- [10] B. A. Mazin. ‘Microwave kinetic inductance detectors’. PhD thesis. California Institute of Technology, 2004.
- [11] C. Song et al. ‘Microwave response of vortices in superconducting thin films of Re and Al’. *Physical Review B - Condensed Matter and Materials Physics* 79.17 (2009), pp. 1–9.
- [12] G. Stan, S. B. Field and J. M. Martinis. ‘Critical Field for Complete Vortex Expulsion from Narrow Superconducting Strips’. *Phys.Rev.Lett.* 92.March (2004), pp. 97003–97004.
- [13] R. Barends et al. ‘Minimal resonator loss for circuit quantum electrodynamics’. *Applied Physics Letters* 97.2 (2010), p. 023508.
- [14] W. D. Oliver and P. B. Welander. ‘Materials in superconducting quantum bits’. *MRS Bulletin* 38.10 (2013), pp. 816–825.
- [15] H. Wang et al. ‘Improving the coherence time of superconducting coplanar resonators’. *Applied Physics Letters* 95.23 (2009), p. 233508.
- [16] D. Niepce. ‘Fabrication and Characterisation of Thin-Film Superconducting Nanowire Superconductors for Novel Quantum Devices’. MA thesis. Chalmers University of Technology, 2014.